

Poleward-Propagating Intraseasonal Monsoon Disturbances in an Intermediate-Complexity Axisymmetric Model

GILLES BELLON

Department of Applied Physics and Applied Mathematics, Columbia University, New York, New York

ADAM SOBEL

Department of Applied Physics and Applied Mathematics, and Department of Earth and Environmental Sciences, Columbia University, New York, New York

(Manuscript received 7 November 2006, in final form 9 April 2007)

ABSTRACT

A model of intermediate complexity based on quasi-equilibrium theory—a version of the quasi-equilibrium tropical circulation model with a prognostic atmospheric boundary layer, as well as two free-tropospheric modes in momentum, and one each in moisture and temperature—is used in a zonally symmetric aquaplanet configuration to simulate aspects of the South Asian monsoon and its variability. Key qualitative features of both the mean state and the 30–60-day mode of the intraseasonal variability are simulated satisfactorily. The model has two limit cycles of similar period and structure that can account for this mode. Both feature northward propagation of the tropical convergence zone from 5°S to 25°N with a period of about 50 days. The dynamics of the oscillations are investigated. The system reaches a Hopf bifurcation when the asymmetry of the sea surface temperature (SST) forcing is increased. Beyond the bifurcation, the mean flow is linearly unstable, and the one linearly unstable mode is similar in structure and period to the nonlinear mode. The wind-induced surface heat fluxes are necessary to obtain the instability of the mean monsoon flow, as are the 2 degrees of freedom in the vertical structure of both humidity and wind.

1. Introduction

The South Asian summer monsoon is characterized by strong intraseasonal variability. Rainy periods over South Asia, called “active phases,” alternate with dry spells, called “breaks,” during the monsoon season (Goswami 2005, and references therein). Since the intensity of the rains does not exhibit a strong intraseasonal variability, the seasonal mean precipitation over the continent depends strongly on the respective durations of these dry and wet phases. Consequently, the interannual variations of the monsoon are also linked to the intraseasonal variability. In particular, the spatial patterns of the intraseasonal variability are similar to those of the interannual variability. Understanding the processes at play in the intraseasonal variation of the monsoon may be relevant to the understanding of the monsoon system at longer time scales. Indeed, a reliable prediction of the monsoon would allow people to

optimize agricultural yields (Gadgil and Rao 2000) and to prepare for extreme events.

During the monsoon, the seasonal mean precipitation field exhibits two longitudinal bands of maximum rain, one over the equator and the other over the monsoon trough around 20°N (Sikka and Gadgil 1980). The intraseasonal variability can be seen as a seesaw between these two tropical convergence zones (TCZs), as shown by the study of composites (Goswami and Mohan 2001). Spectra of intraseasonal variability in precipitation and wind exhibit two dominant modes: the 10–20-day and 30–60-day modes. The 10–20-day mode seems to be associated with disturbances propagating from the Pacific warm pool to South Asia that appear as Rossby waves deviated poleward by the mean monsoon flow (Chatterjee and Goswami 2004; Wang and Xie 1997). On the other hand, the 30–60-day mode is associated with northward propagation of the TCZ from its preferred equatorial position to its preferred monsoon location around 20°N. The onset of the monsoon is associated with such propagating disturbances, and understanding the 30–60-day mode is therefore crucial to the seasonal forecast of the onset.

Corresponding author address: Gilles Bellon, Columbia University, Lamont Campus, 61 Route 9W, Monell Building, Palisades, NY 10964-8000.

E-mail: gilles@iri.columbia.edu

DOI: 10.1175/2007JAS2339.1

About half of these northward-propagating disturbances are associated with the equatorial eastward-propagating Madden–Julian oscillation (MJO; Wang and Rui 1990). Consequently, studies have presented the northward propagation of the tropical convergence zone as a Rossby wave emanating from an MJO Kelvin–Rossby packet (Wang and Xie 1997; Lawrence and Webster 2002). These studies suggest that the northward-propagating TCZ is just the response of the monsoon flow to the forcing of zonally propagating disturbances. But the other half of the northward-propagating disturbances appear independent of zonal propagation, and the 30–60-day mode appears more and more to be a regional phenomenon, that is, perhaps an unstable mode of the monsoon mean flow.

Although some east–west asymmetries seem to play a role in the initiation of the northward propagation over the equatorial Indian Ocean (Jiang and Li 2005; Wang et al. 2006), these propagating disturbances exhibit a high degree of zonal symmetry within a particular longitude band. Zonally symmetric models have therefore been used to improve our understanding of the 30–60-day mode (Webster and Chou 1980; Webster 1983; Goswami and Shukla 1984; Gadgil and Srinivasan 1990; Srinivasan et al. 1993; Nanjundiah et al. 1992; Jiang et al. 2004; Bellon and Srinivasan 2006; Drbohlav and Wang 2005).

In a similar way that the phenomenon of the monsoon itself was at first thought to result primarily from land–sea interaction, continental surfaces were at first considered crucial to the existence of northward propagation (Webster and Chou 1980; Webster 1983), and the scale selection was expected to depend on the land's thermodynamical properties in simple axisymmetric (i.e., zonally symmetric) models (Gadgil and Srinivasan 1990; Srinivasan et al. 1993). Using an axisymmetric general circulation model (GCM), Goswami and Shukla (1984) later showed that northward propagation could occur over the ocean, provided an adequate sea surface temperature (SST) forcing (i.e., with high subtropical SSTs in the summer hemisphere). Although continental surfaces increase the amplitude of the oscillation, the existence of such oscillations appeared to result from convective-dynamical feedbacks (Goswami and Shukla 1984). Furthermore, recent observations have shown that the intraseasonal oscillation has a strong signal in the SST of the Indian Ocean (Sengupta et al. 2001) and coupled modeling studies have shown that the atmosphere–ocean interaction has an important role in modulating the summer intraseasonal variability over South Asia (Fu and Wang 2004). Considerable support has developed for the view that the northward propagation of the TCZ is an intrinsically

atmospheric phenomenon modulated by coupling with oceanic and continental surfaces. How convection and dynamics interact to cause the northward propagation and select its temporal and spatial scales is still unclear.

The work presented here is a step in an attempt to clarify the mechanisms involved in the northward propagation of the TCZ and in the scale selection. Using an aquaplanet intermediate axisymmetric model in summer conditions, we are able to simulate regular oscillations in the 30–60-day range that feature northward propagation of the TCZ. The space and time structures of the model oscillations are very similar to the observed intraseasonal mode. We highlight some of the elements of our model that are necessary to trigger the instability of the monsoon mean flow. In particular, the roles of the asymmetry of the SST forcing and of the wind-induced surface heat fluxes are investigated. The oscillations are also shown to be essentially linear, and the vertical structure appears as the simplest necessary to simulate realistic mean seasonal patterns and intraseasonal oscillations. Further work will examine more closely the mechanisms at play in the propagation, study the role of coupling with the surface (ocean and land), and analyze the scale selection.

Section 2 describes the model we use in this study. Results of the model are presented in section 3 and discussed in section 4.

2. Model

a. Model summary

We use the prototype to the second quasi-equilibrium tropical circulation model (QTCM2) developed by Sobel and Neelin (2006) on the basis of the QTCM1 (Neelin and Zeng 2000; Zeng et al. 2000). The QTCM family of models is based on the Galerkin projection of the primitive equations on a limited number of reference vertical profiles derived from asymptotic solutions of the quasi-equilibrium theory. In QTCM1, the vertical structure of the wind has 2 degrees of freedom (one barotropic mode and one baroclinic mode) and the thermodynamical variables (temperature and humidity) each have 1 degree of freedom. The prototype QTCM2 includes an atmospheric boundary layer (ABL) that adds another degree of freedom for both dynamical and thermodynamical variables.

The model used here further differs from QTCM1 by its axisymmetric equatorial β plane configuration and its physical parameterizations: the radiation is simply represented as a Newtonian cooling, and the Betts–Miller (quasi equilibrium) convective parameterization has been modified to take into account the new thermodynamical degrees of freedom (Sobel and Neelin 2006).

There is one main difference between the model used in this work and the model used in Sobel and Neelin (2006): here, the mixing at the top of the boundary layer is neglected. Sensitivity studies (not shown) show that the mixing at the top of the boundary layer reduces the amplitude of the oscillations without significantly modifying their spatial structure and period. Sufficiently strong mixing at the top of the ABL, such as what might be used if the ABL were considered the subcloud layer of an active shallow convection region, can cause the system to become stable to the oscillations. Such a mixing effectively couples the entire free troposphere to the ABL, while in reality shallow convection couples the subcloud layer to the shallow-cumulus layer, leaving the free troposphere largely decoupled from the ABL. Therefore neglecting the ABL-top mixing appears a reasonable simplification. The ABL and free troposphere remain coupled by deep convection and large-scale vertical advection.

The choice of an aquaplanet configuration is justified by the fact that most intraseasonal activity is located over the oceans (Bellenger and Duvel 2007). We thus implicitly neglect the mechanisms involving continental surfaces, including the differential heating between land and ocean and continental hydrologic feedbacks. Our results will suggest that these mechanisms are not necessary to the existence of the intraseasonal oscillation, except perhaps as they play a role in determining the mean state, which here is determined exclusively by the assumed SST distribution.

The following sections provide details on aspects of the model that are of particular interest for the present study. The reader is invited to refer to the appendix for a complete description of the model.

b. Surface fluxes

Surface fluxes are parameterized by standard bulk formulas:

$$E = \rho_a C_D V_s [q^*(T_s) - q_b] \quad \text{and} \quad (1)$$

$$H = \rho_a C_D V_s (T_s - s_b), \quad (2)$$

where T_s is the SST, $q^*(T_s)$ is the saturation specific humidity at T_s , C_D is the exchange coefficient, ρ_a is the surface air density, and V_s is the surface wind speed. As we are interested in transient solutions here, V_s is taken to be a function of the boundary layer wind \mathbf{v}_b to include wind–evaporation mechanisms (Emanuel 1987; Neelin et al. 1987):

$$V_s = \sqrt{G^2 + |\mathbf{v}_b|^2}, \quad (3)$$

where G is the gustiness, a constant wind that accounts for subgrid circulations; it is set to 5 m s^{-1} . We will investigate the effect of this parameterization of the surface wind in section 3c.

c. SST forcing

In the Indian Ocean, the summer SST is almost uniform between the equator and northernmost shore of the Bay of Bengal and the eastern Arabian Sea, around 20°N . This weak meridional temperature gradient results from summer insolation and oceanic transport, in particular from the absence of poleward oceanic heat transport due to the presence of the Asian continent. In the west Pacific, the SST exhibits a similar pattern, and the surface temperature over India is very similar to that of the neighboring seas. We use an SST profile close to the observed Indian Ocean's July–September average up to its northern shore (20°N). Observed continental temperatures exhibit a small peak around 25°N . Further north, the surface boundary condition is strongly influenced by the topography of the Himalayan highlands, which we do not attempt to model here. A sensitivity study showed that our results are not sensitive to the details of the surface temperature distribution poleward of 25°N . We present results using the following idealized SST forcing:

$$\begin{aligned} \text{if } -\sigma_y < y < 0, & \quad \text{SST} = \text{SST}_{\text{max}} - \Delta\text{SST} \sin^2\left(\frac{y}{2\sigma_y} \pi\right); \\ \text{if } 0 < y < y_0, & \quad \text{SST} = \text{SST}_{\text{max}}; \\ \text{if } y_0 < y < y_0 + \sigma_y, & \quad \text{SST} = \text{SST}_{\text{max}} - \Delta\text{SST} \sin^2\left(\frac{y - y_0}{2\sigma_y} \pi\right); \\ \text{otherwise,} & \quad \text{SST} = \text{SST}_{\text{max}} - \Delta\text{SST}. \end{aligned} \quad (4)$$

Here, y_0 is the latitudinal extent of the flat maximum of SST at SST_{max} , σ_y is the latitudinal extent of the poleward SST decrease on each side of the tropical plateau, and ΔSST is the equator–pole SST difference. In the

control runs, the SST parameters are set as follows: $(\text{SST}_{\text{max}}, \Delta\text{SST}) = (29^\circ\text{C}, 31^\circ\text{C})$ and $(y_0, \sigma_y) = (2000 \text{ km}, 7000 \text{ km})$. (This SST field is illustrated and discussed below.)

TABLE 1. Model parameter values.

Parameter	Value	Definition
p_s, p_e, p_t	1000, 900, 150 hPa	Pressures at nominal surface, ABL top, and model top (tropopause)
$\langle a_1 \rangle^F, a_{1e}$	0.4243, 0.2931	Vertical mean and ABL top value of temperature basis function
$\langle b_1 \rangle^F, b_{1e}$	0.2406, 0.7576	Vertical mean and ABL top value of moisture basis function
$\langle a_1^+ \rangle^F$	0.2445	
$\langle a_b^+ \rangle^b, a_b^{+e}$	0.0512, 0.1038	
$\langle V_1^2 \rangle^F, \langle V_1^3 \rangle^F$	$3.67 \times 10^{-2}, 3.2 \times 10^{-3}$	
V_{1e}	-0.2121	ABL top value of baroclinic basis function
q_{re}, T_{re}	38.925 K, 296.65 K	ABL top reference moisture and temperature
q_{rb}, s_{rb}	51.96 K, 302.00 K	ABL reference moisture and dry static energy
M_{sr1}, M_{sr0}	3.60 K, 16.34 K	Reference dry static stabilities
M_{sp1}, M_{sp0}	$4.05 \times 10^{-2}, 0.188$	Dry static stability changes per T_1 change
M_{rq1}, M_{qr0}	3.00 K, 28.05 K	Reference gross moisture stratifications
M_{qp1}, M_{qp0}	$3.78 \times 10^{-2}, 0.516$	Gross moisture stratification changes per q_1 change
ϵ_1	$8.77 \times 10^{-7} \text{ s}^{-1}$	Frictional damping rate on baroclinic mode
ϵ_b	$2.20 \times 10^{-5} \text{ s}^{-1}$	ABL drag coefficient
τ_c	0.3 day	Convective time scale
σ	0.2	Constant partitioning between convective cooling and drying of ABL
T_R, τ_R	-50 K, 15 days	Radiative equilibrium temperature and time scale
Q_{Rb0}, τ_{Rb}	$-1.5 \text{ K day}^{-1}, 2 \text{ days}$	ABL radiative background heating and time scale
ρ_a, C_D	$1 \text{ kg m}^{-3}, 1.5 \times 10^{-3}$	Surface air density, exchange coefficient
k_q, k_v	$8 \times 10^5, 2 \times 10^5 \text{ m}^2 \text{ s}^{-1}$	Diffusivities for moisture and velocity

d. Simulation design and numerics

The equations are solved using a leapfrog differencing in time with a Robert–Asselin filter and finite differences in space. The equations for the free-tropospheric baroclinic variables are solved in advective form using first-order upwind differencing and the barotropic and ABL equations are solved in flux form with a centered scheme.

The model is integrated over a domain of 20 000 km (10 000 km in each hemisphere), with a time step of 20 s and a spatial resolution of 50 km (400 grid points). As 1° of latitude roughly equals 100 km, the latitude will be either given in degrees or kilometers. Increasing the temporal and spatial resolutions does not significantly alter the results. The model is integrated in time until it reaches a steady state or a limit cycle (as determined by simple inspection).

Table 1 shows the parameters used in the present study, which are very similar to the parameters used in Sobel and Neelin (2006).

3. Results

a. Control runs

Simulations with different initial conditions were performed, and it appeared that the model reaches one of two limit cycles depending on these initial conditions. The two limit cycles exhibit similar, realistic mean states and northward propagation of the rain anomaly.

The limit cycle of smaller amplitude will be called LC1 and the other will be labeled LC2.

1) MEAN STATES

Figures 1, 2, and 3 show the time averages of the different variables for those two regimes. For simplicity, Fig. 2 shows the winds at the tropopause $\mathbf{v}_t = \mathbf{v}_0 + V_{1t}\mathbf{v}_1$ [with $V_{1t} = V_1(p_t)$] and the wind just above the boundary layer top $\mathbf{v}_e = \mathbf{v}_0 + V_{1e}\mathbf{v}_1$. For both limit cycles, the precipitation exhibits two maxima, one over the equator and the other around 20°N ; we will refer to the latter as “monsoonal” (see Fig. 1). These two maxima correspond to two TCZs separated by a region of moisture divergence (i.e., with less precipitation than evaporation). The precipitation minimum is more pronounced in LC2 than in LC1. This precipitation pattern is typical of a monsoon situation (Sikka and Gadgil 1980).

The dynamical fields also show a strong qualitative similarity with the observed summer fields above the Indian Ocean: a strong subtropical jet around 25°S and westward flow at the equator and in the northern tropics (Figs. 2b), a reversal of the ABL zonal wind across the equator (Fig. 2f), and a northward flow in the lower levels with a return flow in the upper troposphere (Figs. 2a, 2c, and 2e). Note that, in this model, the upper-tropospheric meridional wind has a minimum around the equator (Fig. 2a) and a collocated maximum of middle-tropospheric wind (Fig. 2c), which is associated with baroclinic divergence (i.e., divergence in the upper

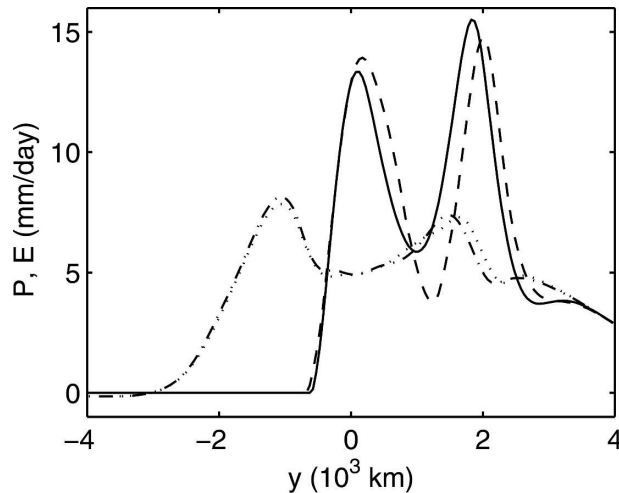


FIG. 1. Mean states of the model in the control runs: precipitation for the first limit cycle (solid) and the second limit cycle (dashed), and evaporation for LC1 (dash-dotted) and LC2 (dotted).

troposphere and convergence in the lower free troposphere) in the northern tropics and baroclinic convergence in the southern tropics. On the other hand, the boundary layer wind exhibits a minimum over the equator with one maximum in each hemisphere (Fig. 2e). This yields two regions of barotropic divergence (i.e., convergence in the boundary layer and divergence in the free troposphere) separated by a region of barotropic convergence between the equator and 15°N . This convergence pattern is essential to the existence of the region of moisture divergence mentioned above, and therefore to the existence of two distinct TCZs and the associated precipitation maxima. The two maxima of v_b are related to the existence of weak cross-equatorial flow in the boundary layer that can be explained by weak gradients of temperature on the equator, where the Coriolis force vanishes (Pauluis 2004). While the mean states of the two modes are very similar in the Southern Hemisphere and in the middle latitudes, they differ slightly in the monsoon region. In particular, the structure of u_b and v_b are slightly displaced poleward in LC2 relative to LC1.

The mean humidity and temperature fields are also very similar in structure to those observed during the South Asian monsoon. The mean humidity exhibits two maxima in both the boundary layer and the free troposphere (Figs. 3a and 3c). Their locations roughly correspond to those of the precipitation maxima, although the southernmost maximum of q_b is clearly south of the equator compared with the precipitation maximum (Fig. 3c): this results from strong local evaporation in a region of suppressed deep convection. For each mode,

the separation between the maxima of q mirrors the separation between the TCZs (Figs. 2a and 3a). The mean free-tropospheric temperature exhibits a smooth maximum in the monsoonal TCZ over the otherwise flat tropical temperature (Fig. 3b). In the boundary layer, the mean dry static energy has two maxima collocated with the maxima in q_b (Fig. 3d). The mean thermodynamical variables have very similar structures in the two limit cycles, although the features in LC2 are more prominent in the boundary layer and somewhat weaker in the free troposphere than their counterparts in LC1.

Considering its simplicity, the model reproduces the summer mean flow in the Asian region very well. This skill by itself is remarkable, since no tuning was done to achieve it, and considering that the effects of land, topography, and deviations from axisymmetry are all neglected.

2) OSCILLATIONS

Figure 4 shows the time evolution of precipitation in LC1. The total precipitation exhibits a seesaw between the equatorial and the monsoonal TCZ (Fig. 4a). On the other hand, the precipitation anomaly shows clear northward propagation of rain (Fig. 4b), as in the observed records (Sikka and Gadgil 1980). The amplitude of the oscillation is larger in the monsoonal TCZ than over the equator. This suggests that this model can account for some of the basic mechanisms that cause the succession of drought and violent rains during the monsoon season over the Asian continent. The period of the oscillation is 51.2 days, within the 30–60-day range of the slower mode of the observed intraseasonal variability of the monsoon.

The time evolution of the precipitation and its anomaly for LC2 is shown in Fig. 5. LC2 shows a strong similarity with LC1 in terms of the alternating rain between the two TCZs and the northward propagation of the precipitation anomalies, but the amplitude of the oscillations is about 50% larger in the TCZs in LC2 compared with LC1. Considering the similar mean precipitation fields, this results in shorter periods of stronger precipitation and longer periods of drought (the vertical straight lines in Fig. 5b indicate nonprecipitating periods when the anomaly is constant and equals the opposite of the mean), that is, more extreme events in LC2. The period of this mode, 50.3 days, is similar to that of LC1. For both LC1 and LC2, the propagation appears to be in two parts separated by a minimum of the precipitation anomaly near the location of the minimum in the mean precipitation, around 10°N . In LC2, this separation appears more clearly because the precipitation anomalies between 5°S and 10°N are larger

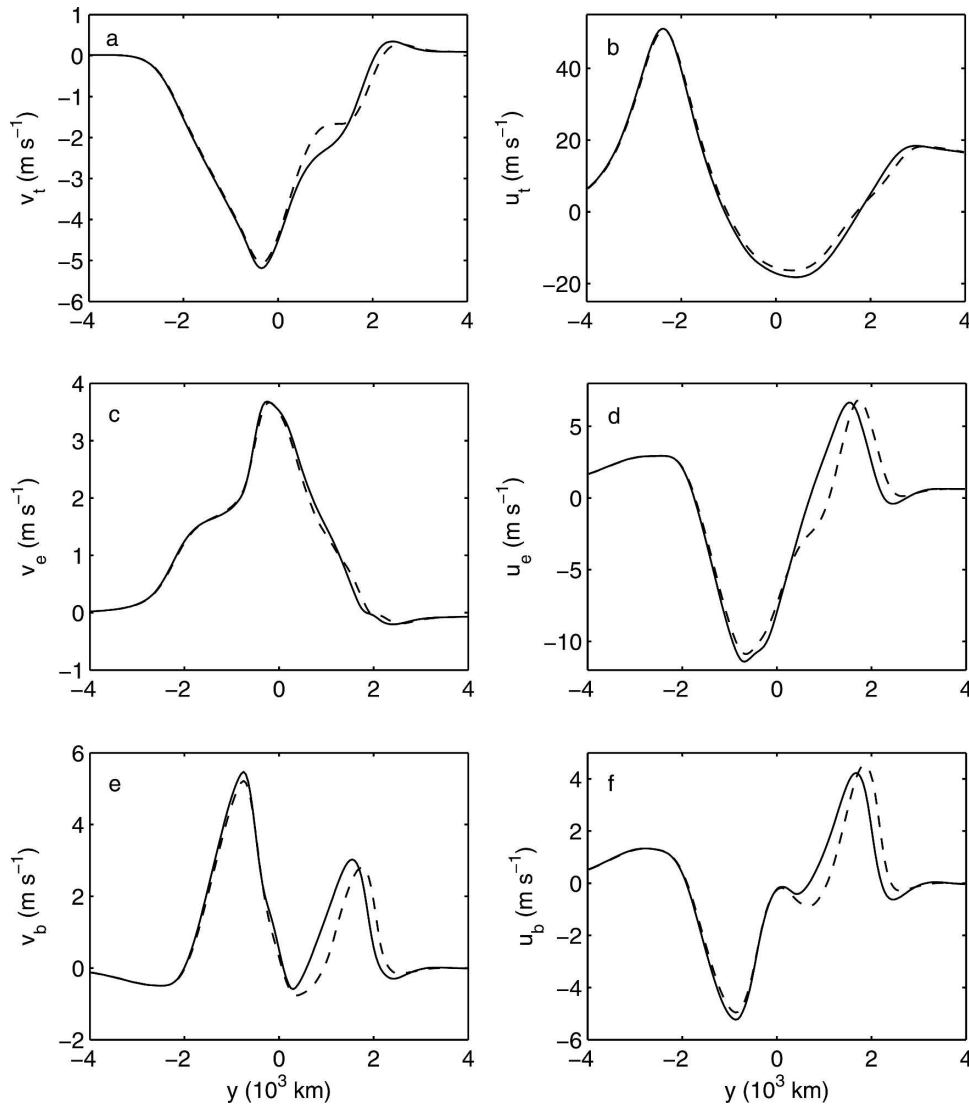


FIG. 2. Mean states of the model in the control runs for LC1 (solid) and LC2 (dashed): wind (a), (b) at the tropopause; (c), (d) above the boundary layer; and (e), (f) in the boundary layer.

than in LC1. The two parts of the propagation are also characterized by different propagation speeds: while the precipitation anomalies propagate at a speed of about 1.5 m s^{-1} between 5°S and 10°N , their propagation slows down to about 0.7 m s^{-1} between 10° and 25°N (for both LC1 and LC2).

Both oscillatory modes have dynamical structures that are qualitatively similar to composites of observations and reanalysis. First, a maximum of boundary layer convergence (i.e., a maximum of barotropic divergence) appears a few degrees north of the maximum of precipitation in the composites (Jiang et al. 2004; Goswami 2005), at least for latitudes larger than 5°N (Kemball-Cook and Wang 2001). Figures 6b and 7b show that this is the case in our model. Nevertheless,

for $y > 1500 \text{ km}$, the distance between the maximum of barotropic divergence and that of precipitation decreases until they become collocated at the northern end of the propagation around $y = 2000 \text{ km}$. Furthermore, a maximum of upper-tropospheric divergence follows the maximum of convection (Jiang et al. 2004); and this is reproduced by the maximum of baroclinic divergence a few degrees south of the precipitation maximum in our model (Figs. 6a and 7a). Although the structure of LC2 is more intricate than that of LC1, the patterns are similar. The amplitudes of the divergences are larger in LC2 than in LC1, mirroring the amplitude of the precipitation.

Previous studies have well documented that these observed divergence patterns are associated with a maxi-

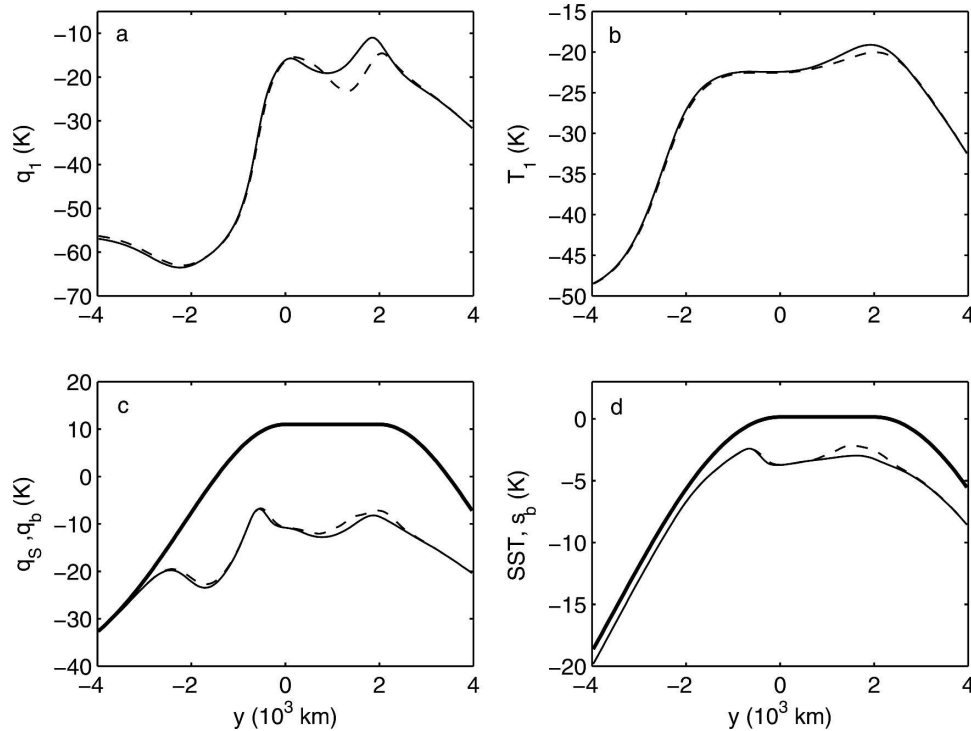


FIG. 3. Mean states of the model in the control runs for LC1 (solid) and LC2 (dashed): (a) humidity and (b) temperature in the free troposphere, and (c) humidity and (d) static energy in the boundary layer. Thick lines show the SST (d) and the corresponding saturation humidity (c).

mum of vorticity collocated with, or slightly north of the maximum of barotropic divergence (Jiang et al. 2004; Goswami 2005). This vorticity pattern extends over the whole troposphere, with a maximum in the middle troposphere (Jiang et al. 2004), and causes the barotropic divergence pattern described above via frictional convergence (in the boundary layer) and Coriolis acceleration in the free troposphere (Jiang et al. 2004; Goswami 2005). In LC1, a maximum in boundary layer vorticity is located north of the maximum in barotropic divergence, while a maximum in barotropic vorticity and a minimum in baroclinic vorticity are almost collocated with the maximum in barotropic divergence (Fig. 8). Considering the vertical profiles V_0 and V_1 , these extrema translate into a maximum of vorticity with maximum amplitude in the middle troposphere and a weak vorticity at the tropopause (considering that $V_{1t} = 0.3$). This pattern is very similar to the composite reanalyzed vorticity (Jiang et al. 2004).

Figure 9 shows the time evolution of the vorticity associated with the baroclinic and barotropic velocity modes in LC2. The patterns are more intricate and the amplitudes are larger than in LC1, but the general structure of the mode is similar. Furthermore, the phase relation between divergences and vorticities is qualita-

tively the same as in LC1, and thus similar to the composites of observations and reanalysis.

b. Bifurcations

Further simulations are performed to understand the existence of the two modes. The latitudinal extent of the flat maximum of SST, y_0 , is taken as the control parameter, because it allows for the study of the transition between the mean Hadley circulation, symmetric about the equator, to the monsoon circulation. Increasing y_0 results in increasing both the energy input—by expanding the surface of high SST—and its asymmetry with respect to the equator. Here y_0 is systematically varied from 0 to 3000 km, but different initial conditions are sampled to populate the two limit cycles. Using the final state of a previous simulation with a similar value of y_0 as initial conditions, the model is integrated in time until it reaches a steady state or a limit cycle, therefore only the stable branches of the bifurcation tree are explored. The amplitude of each mode is defined as the peak-to-peak amplitude of precipitation anomaly at the latitude where this amplitude is the largest (in the monsoonal TCZ for all the cases presented here).

Figure 10a shows the bifurcation diagram for $y_0 >$

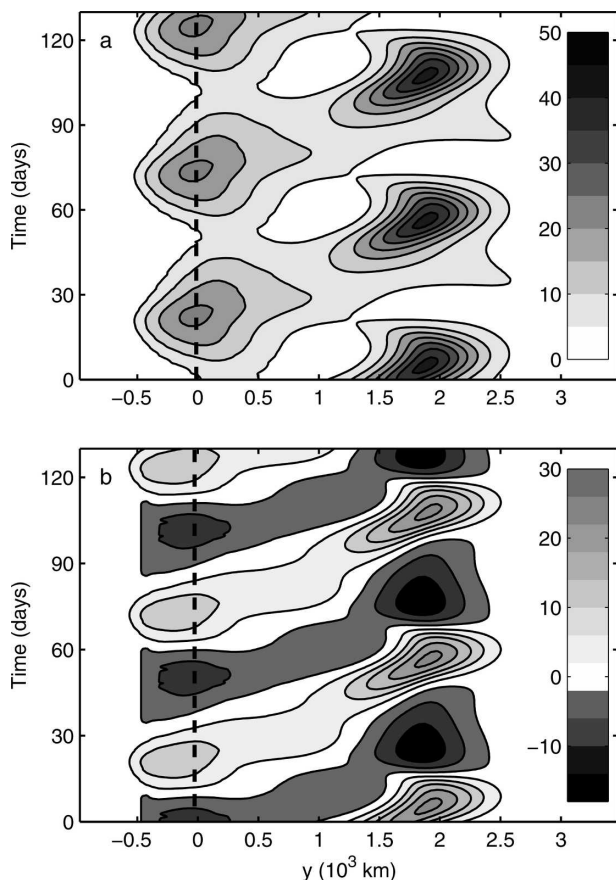


FIG. 4. (a) Precipitation and (b) precipitation anomaly in the first limit cycle (in mm day^{-1}).

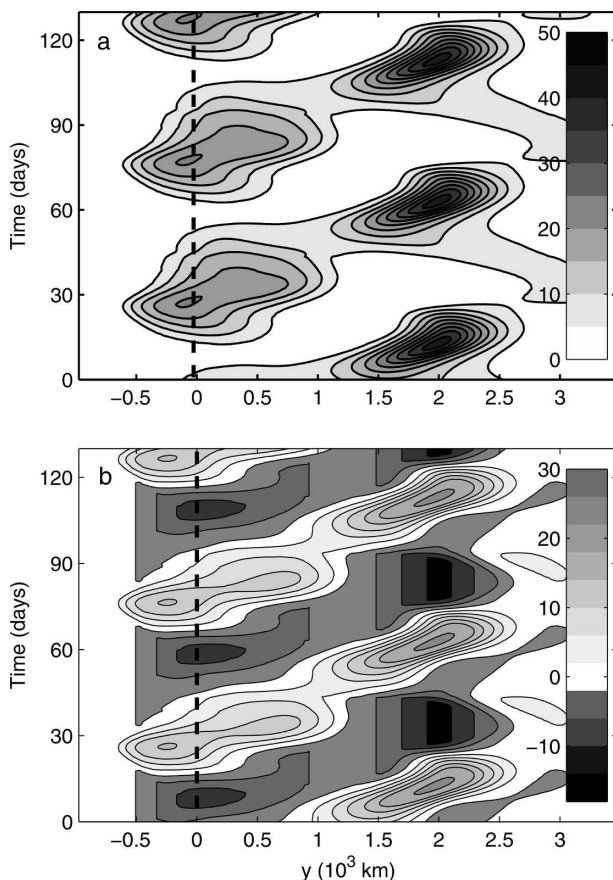


FIG. 5. (a) Precipitation and (b) precipitation anomaly in the second limit cycle (in mm day^{-1}).

1000 km. For $y_0 \leq 1500$ km, the model has a stable steady state. At $y_{0c} \approx 1500$ km, the model exhibits a Hopf bifurcation: the steady state becomes unstable and LC1 appears, with an amplitude that scales with $\sqrt{y_0 - y_{0c}}$. At $y_{0c1} \approx 1900$ km, LC2 appears with a larger amplitude than LC1, and at $y_{0c2} \approx 2480$ km, LC1 becomes unstable. This shows that another bifurcation occurs, and most probably a saddle node bifurcation: an unstable limit cycle is likely to connect LC1 and LC2 for $y_{0c1} < y_0 < y_{0c2}$. Sensitivity studies show that the exact values of y_{0c} , y_{0c1} , and y_{0c2} are model dependent. For example, using the centered vertical advection scheme instead of the upwind one leads to $y_{0c} \approx 1000$ km. The structure of the bifurcation is nevertheless robust.

Over the domain of y_0 we investigated, the periods of both oscillatory modes are not very sensitive to the extent of the SST forcing and remain in the 50-day range (Fig. 10b). Furthermore, the dynamical structure of the oscillations is very similar to the control cases (not shown).

Our results show that, provided the equatorial maxi-

mum of SST extends sufficiently far poleward, the mean monsoon flow is unstable and gives rise to two possible oscillatory modes. Northward propagation of the TCZ can thus occur without stimulation by zonally propagating disturbances, and in this model, land–sea interaction is not involved in the basic instability mechanism.

Figure 11 shows the values and locations of the precipitation maxima. For a small y_0 (< 400 km), the steady state has only one maximum of very intense precipitation close to the equator. For larger y_0 , the steady (or mean) state of the model exhibits two maxima of moderate precipitation similar to the control results. The monsoonal precipitation maximum is more intense than the equatorial maximum in LC1 and up to $y_0 \approx 2500$ km in LC2. After the second precipitation maximum appears, the equatorial rainband stays very close to the equator. On the other hand, the increase of the latitude of the monsoonal maximum of precipitation with y_0 is highly nonlinear (Fig. 6b): for y_0 around 400 km, this maximum splits from the equatorial rainband and reaches latitudes of 10° – 12°N within a small range of y_0 .

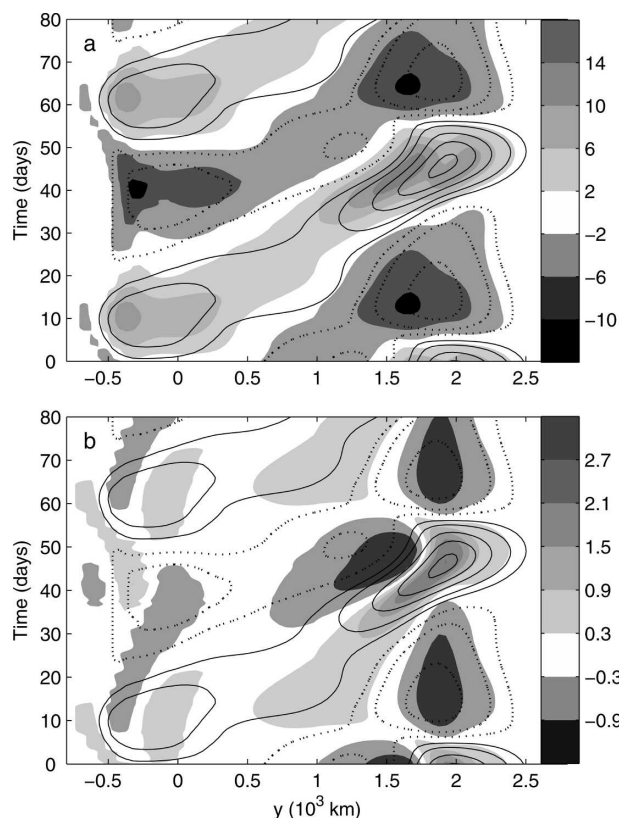


FIG. 6. Shaded areas indicate anomalous (a) baroclinic and (b) barotropic divergences in the first limit cycle (in 10^{-6} s^{-1}). Contours of positive (solid) and negative (dashed) precipitation anomalies are reproduced.

This might explain part of the suddenness in the latitudinal shift of the TCZ during monsoon onset, although given how sudden the onset is, we expect processes that are not in quasi-equilibrium with the SST to play an important role in the onset (Mapes et al. 2005). For $500 \text{ km} < y_0 < 1500 \text{ km}$, the latitude of the monsoonal precipitation maximum increases weakly. For larger y_0 , the latitude of the monsoonal rain peak increases with the amplitude of the oscillation in both LC1 and LC2. The extent of the latitudinal propagation follows closely the location of the monsoonal precipitation maximum (not shown).

Overall, in this model, the existence of a double TCZ does not intrinsically result from the northward propagation of the equatorial rainband: the mean state of LC1 for y_0 slightly greater than that for which the model is neutrally stable is very similar to the steady state for y_0 slightly smaller than that value, and both exhibit two precipitation maxima. Nevertheless, the oscillatory modes make the monsoonal maximum penetrate further into the northern subtropics.

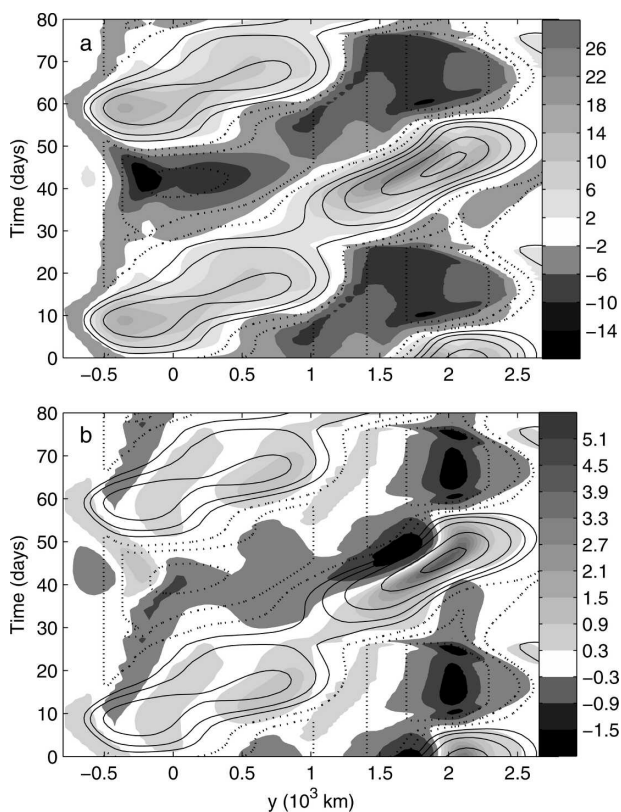


FIG. 7. Shaded areas indicate anomalous (a) baroclinic and (b) barotropic divergences in the second limit cycle (in 10^{-6} s^{-1}). Contours of positive (solid) and negative (dashed) precipitation anomalies are reproduced.

c. Role of wind-induced surface fluxes

The dependence of the surface fluxes on the surface wind is a candidate for explaining aspects of the intraseasonal variability. These processes are named wind-induced sea-air surface heat exchange (WISHE) or wind-evaporation feedback (Emanuel 1987; Neelin et al. 1987). To investigate the role of this feedback on the oscillatory modes in our model, we remove the intraseasonal variations of the boundary layer wind in the expression of V_s :

$$V_s = \sqrt{G^2 + |\overline{\mathbf{v}_b}|^2}, \quad (5)$$

where the overbar refers to the time mean of the variable over a period in the control run.

An additional simulation is performed, with $|\overline{\mathbf{v}_b}|$ computed from the control run for LC1, and we name it NoW. The simulation leads to a steady state. The wind-induced surface fluxes appear to be necessary to the instability of the monsoon flow, as in the case of some simple models of the zonally propagating MJO and some GCM simulations (Maloney and Sobel 2004;

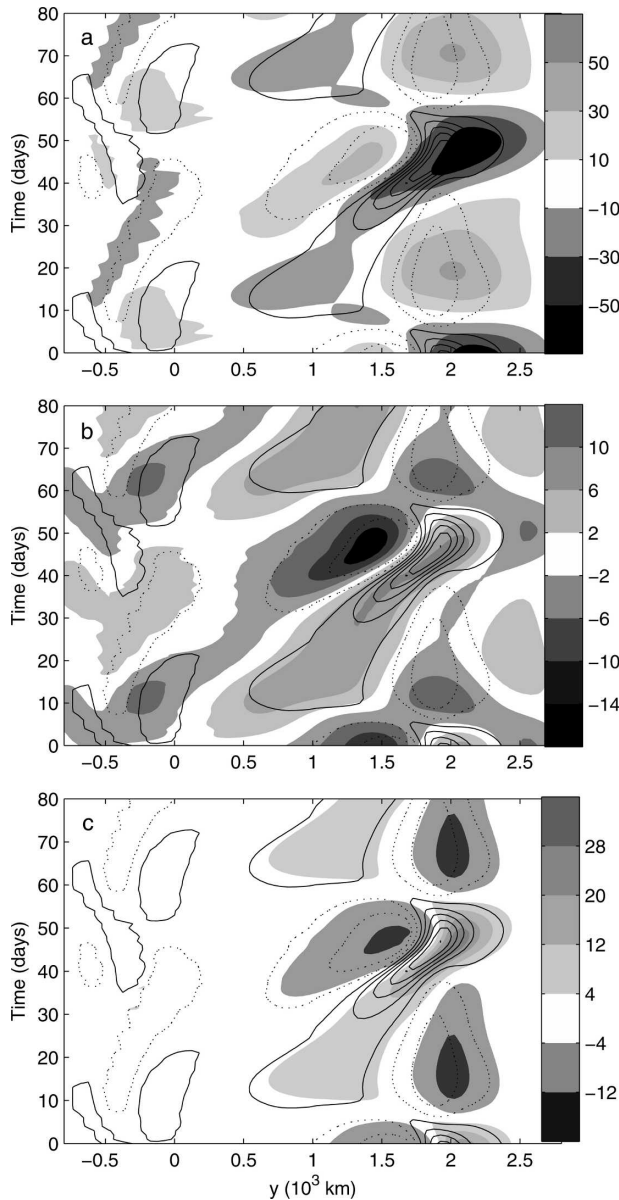


FIG. 8. Shaded areas indicate anomalous (a) baroclinic, (b) barotropic, and (c) boundary layer vorticities in the first limit cycle (in 10^{-6} s^{-1}). Contours of positive (solid) and negative (dashed) barotropic divergence anomalies are reproduced.

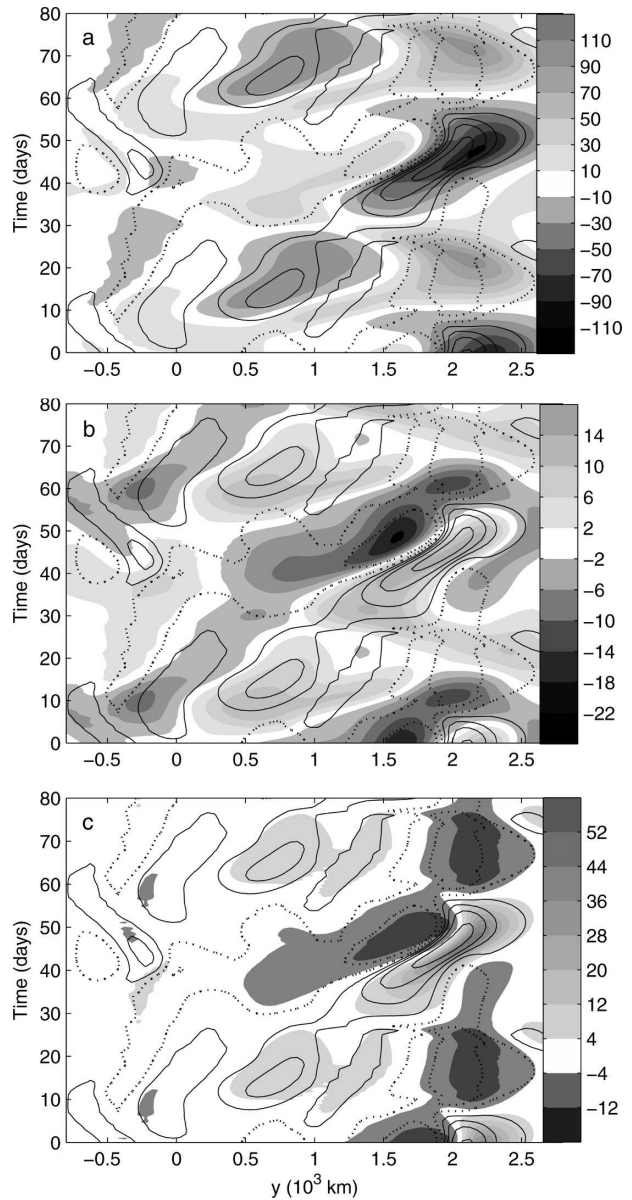


FIG. 9. Shaded areas indicate anomalous (a) baroclinic, (b) barotropic, and (c) boundary layer vorticities in the second limit cycle (in 10^{-6} s^{-1}). Contours of positive (solid) and negative (dashed) barotropic divergence anomalies are reproduced.

Neelin et al. 1987). Figure 12 shows the precipitation and surface fluxes in the control run and in NoW. While the sensible heat flux is similar in the two simulations, the evaporation in the monsoonal TCZ is significantly smaller in NoW than in the control run. In this region, the control-run variability of V_s is almost in phase opposition with that of the ABL humidity. This causes an additional energy input in the atmosphere that participates in the development of the instability. In the control case, the monsoonal TCZ is a few degrees north of

its NoW counterpart (Fig. 12a): the additional evaporation is advected northward by the boundary layer flow, and this creates the conditions for deep convection further north than in the NoW case. This marginal effect (already noted in section 3b) is the only influence of the intraseasonal oscillation on the seasonal pattern of rainfall in our model.

These results hold for stronger forcings (y_0 up to 3000 km—not shown); the same computation using the mean state of LC2 yields similar results (not shown).

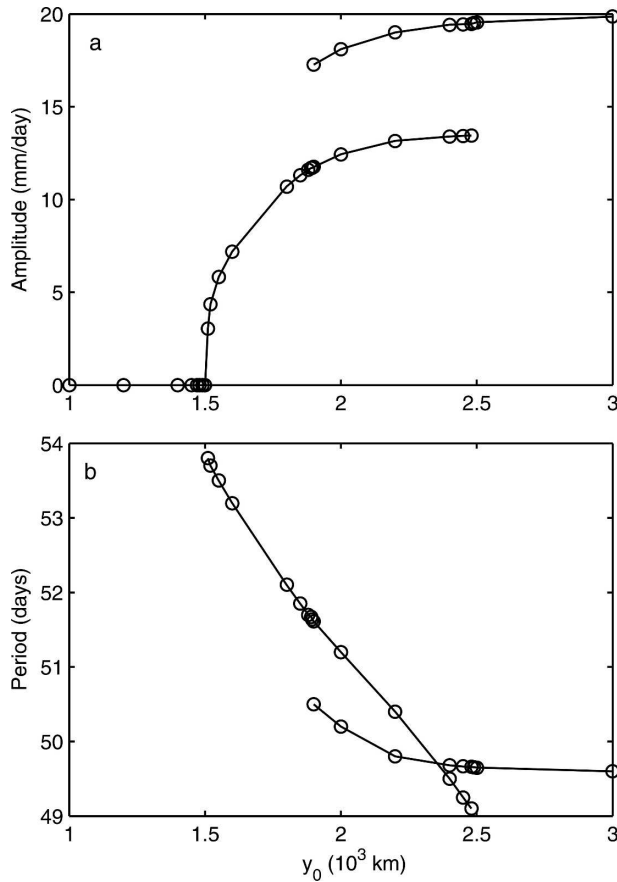


FIG. 10. Bifurcation diagram of the model: (a) amplitude and (b) period of the oscillation. The circles indicate actual computations of the model.

This shows that the wind–evaporation feedback is structurally crucial to the instability of the monsoon flow in our model. Because of the importance of surface fluxes in our atmospheric model, ocean–atmosphere coupling is likely to strongly modulate the intraseasonal oscillation in our model, as it does in GCMs (Fu and Wang 2004). The model used here does not include the ocean–atmosphere coupled processes, and inclusion of these could modify the role of the wind-induced surface fluxes: SST perturbations associated with these surface-flux anomalies can modulate the fluxes and might reduce the sensitivity of our model’s oscillation to the wind-induced effect. Further work will address these issues.

d. Nonlinear oscillation and linear mode

The amplitude of the oscillations in LC1 and LC2 are of the same order of magnitude as the mean fields. This suggests that the mechanisms of the oscillations are strongly nonlinear. On the other hand, previous studies

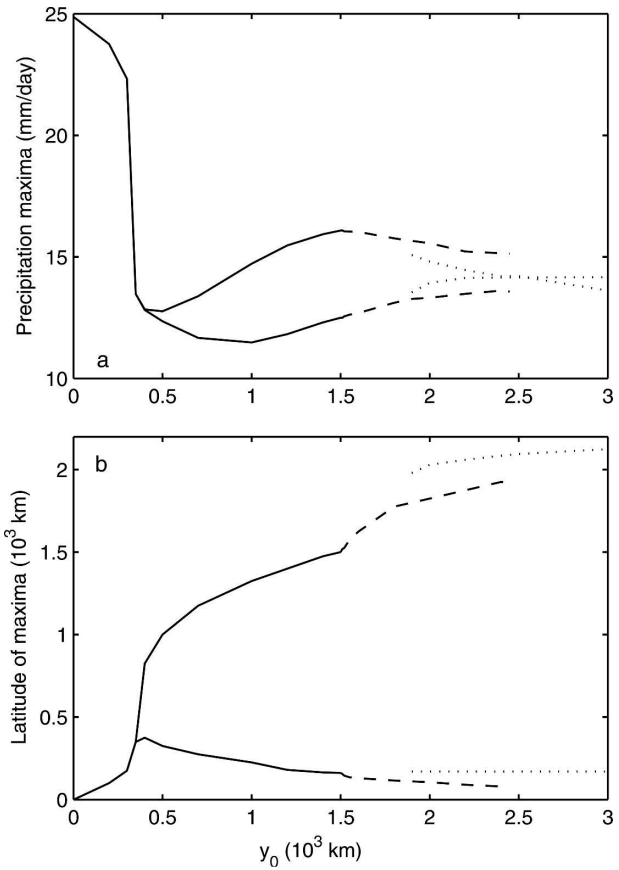


FIG. 11. (a) Precipitation maxima and (b) their latitudinal location for the steady-state cases (solid), LC1 (dashed), and LC2 (dotted).

of both the 10–20-day mode (Chatterjee and Goswami 2004) and the 30–60-day modes (Drbohlav and Wang 2005) simulated part of the intraseasonal variability using linear (or almost linear) models. At least one of the limit cycles in our model may result from the nonlinear saturation of the growth of a linearly unstable mode with similar structure and period. To investigate whether the dynamics of these oscillations are exclusively nonlinear or essentially linear, we compare the results of the nonlinear simulations with the eigenmodes of a linearized version of the model. To facilitate the comparison, we first decompose the precipitation in LC1 into a sum of harmonics:

$$P(y, t) = \bar{P}(y) + \sum_{n=1}^{\infty} P_n(y) \cos\left(2\pi \frac{t}{nT} - \Phi_n\right), \quad (6)$$

where the overbar refers to the time mean of the variable over a period in the control run. Here P_n is the amplitude of the n th harmonic and Φ_n is its phase (counted as a lag from the time of maximum precipitation at the equator); T is the period of LC1 (51.2 days).

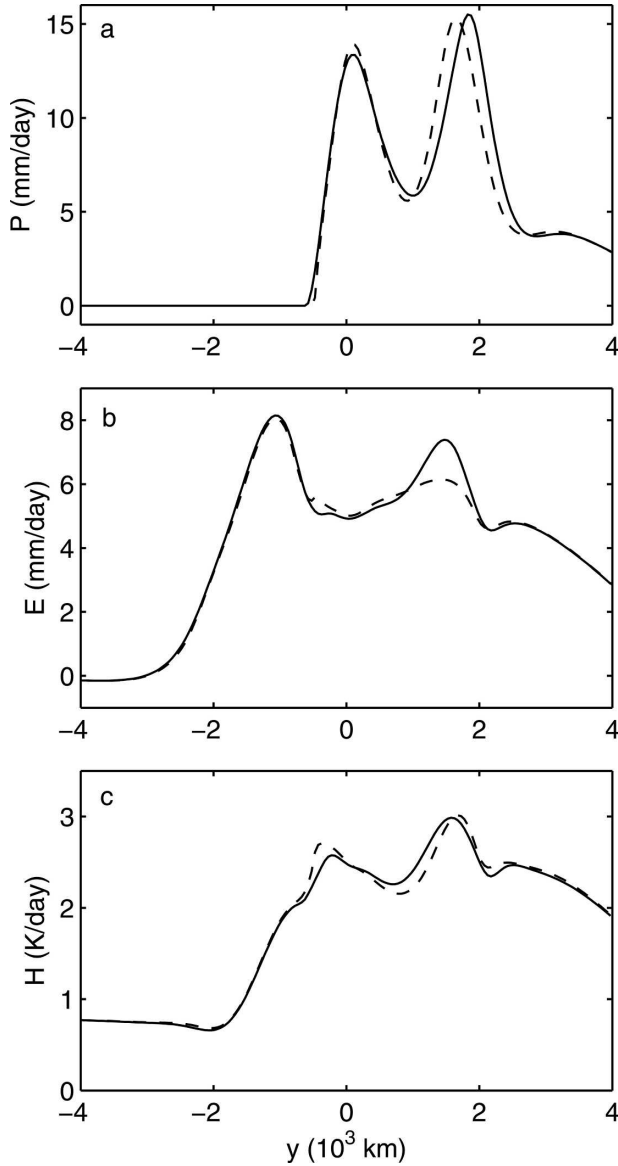


FIG. 12. (a) Precipitation, (b) evaporation, and (c) sensible heat flux for simulation NoW (dashed) and the corresponding the control run (LC1, solid).

Figure 13 shows the first three harmonics of P ; the other harmonics have negligible amplitudes. The amplitude of the first harmonic is much larger than those of the two following harmonics. Furthermore, the first harmonic accounts for most of the characteristics of the oscillation: it exhibits two maxima of amplitudes in the two TCZs (Fig. 13a) and northward propagation from the equator to 20°N (Fig. 13b). If linear dynamics control the structure and dynamics of the nonlinear oscillations, we expect the structure in amplitude and phase of the most unstable linear mode to match that of the dominant harmonic.

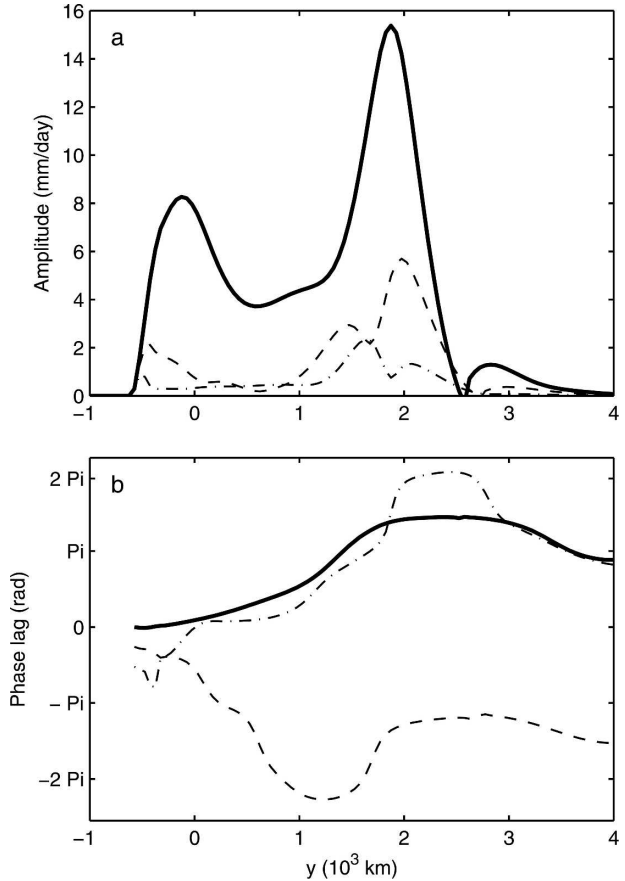


FIG. 13. (a) Amplitude and (b) phase of the first three harmonics of precipitation in LC1 (thick: first harmonic; dashed: second harmonic; dash-dotted: third harmonic).

To check whether this is the case, we develop a linearized version of our model. For the sake of brevity, the equations of this linear model are not explicitly stated in this paper. They can be obtained by a straightforward linearization of the nonlinear equations. The only possible subtleties are those involving the convective tendencies and the vertical advection at ABL, both of which are inherently nonlinear (if the upwind scheme is used for the vertical advection). The perturbation of precipitation is taken proportional to the convective available potential energy: $P' = \epsilon_c \mathcal{E}'$, and the linearized convective tendencies are given by

$$\begin{aligned} \langle Q_c \rangle^{F'} &= \epsilon_c \langle a_1 \rangle^F (h'_b + \delta h'_b - T'_1), \\ \langle Q_q \rangle^{F'} &= \epsilon_c \langle b_1 \rangle^F (h'_b + \delta h'_b - q'_1), \\ \langle Q_c \rangle^{b'} &= \epsilon_c \sigma \delta h'_b, \quad \text{and} \\ \langle Q_q \rangle^{b'} &= \epsilon_c (1 - \sigma) \delta h'_b; \end{aligned} \quad (7)$$

where primes indicate the deviation from the basic state. This is equivalent to taking $\mathcal{H} = 1$ for the perturbation convective contributions even where \mathcal{E} is nega-

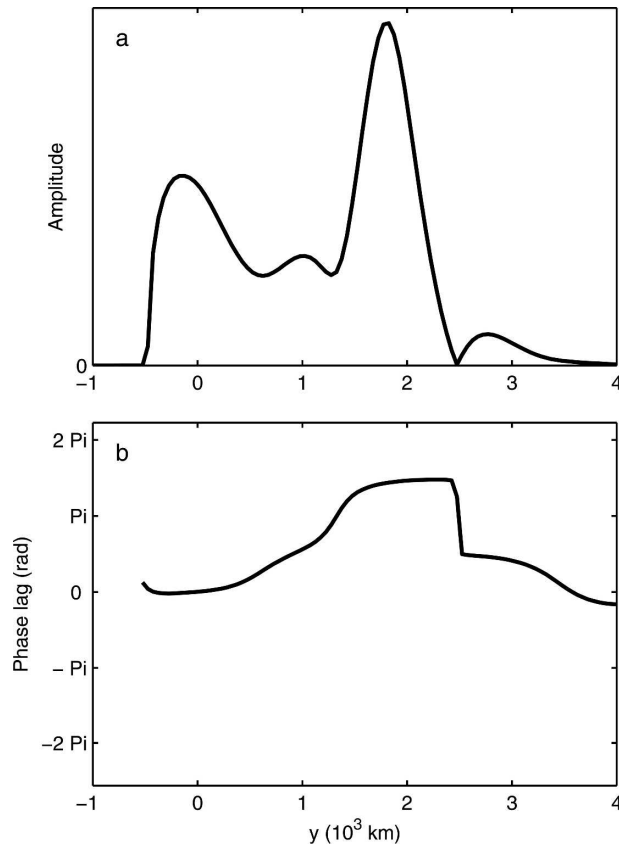


FIG. 14. (a) Amplitude and (b) phase of the unstable mode of the linear model.

tive, a common approximation (Jiang et al. 2004; Goswami and Mohan 2001). It is the main difference with the model used in Drbohlav and Wang (2005), where the positive-only criterion is applied to the precipitation perturbation. This nonlinearity explains why their model does not produce exponentially growing (or decaying) modes as would be expected from a linear model.

In our linear model, the centered scheme is implemented in place of the upwind scheme for the vertical advection at the top of the ABL, and the mean state of LC1 is used as the basic state about which we linearize. The eigenvalues and eigenvectors of the model Jacobian matrix are numerically computed using the same spatial resolution as in the control case (400 grid points). This Jacobian matrix has only one unstable eigenvector. This unstable eigenvector is an oscillatory mode that is well separated from the others damped modes, with an e -folding time scale of 51.5 days and a period of 63.3 days. Figure 14 shows the spatial structure of this mode in amplitude and phase.

The similarity of the structure and period of the linear mode with the first harmonic of the nonlinear limit

cycle is striking. The linear mode features two maxima of amplitude in the TCZs and a northward propagation from the equator to 20°N . The difference in period results mostly from (i) the simplification of the relationship between precipitation and \mathcal{E} (computations using a linearized, smoothed function \mathcal{H} lead to an unstable mode with a 55.2-day period), and (ii) the use of the centered scheme for the advection at the top of the boundary layer: the nonlinear model with centered scheme has a limit cycle with a period of 55 days (not shown). However, it also exhibits small differences such as an additional maximum around 10°N , and phase opposition with the first harmonic of LC1 north of 25°N . Despite these differences, it appears that the linear dynamics of the system are sufficient to explain most of the characteristics of the propagating monsoon disturbances in our model. This allows us to investigate the sensitivity of the oscillation to parameters, such as the convective and radiative time scales, without changing the mean flow. The role of the mean flow itself can be studied. Such sensitivity experiments will be used in future work to further understand the scale selection and other properties of the disturbances.

e. Role of the second degree of freedom in the vertical structure

If our goal is to extract the fundamental mechanism of a given phenomenon, it is desirable to use the simplest model possible to simulate it. In the present case, it is reasonable to ask whether we are in fact using the simplest possible model, or whether the QTCM1, which lacks an explicit ABL but is otherwise quite similar to our model, would behave in an essentially similar way. The answer to this question will tell us what the role of the ABL is in the simulated oscillations, and perhaps, by extension, in those observed in the atmosphere. Previous studies (Jiang et al. 2004; Drbohlav and Wang 2005) suggest that this role is important.

First, we run the QTCM1 with the same monsoon forcings as described in section 2. The use of the QTCM1 in such an axisymmetric configuration has given some insights into the behavior of the Hadley circulation (Burns et al. 2006). The QTCM1 reaches a steady state in a few weeks: it is unable to reproduce the low-frequency variability that we obtain in the prototype QTCM2. Figure 15 shows the precipitation and evaporation of the QTCM1 monsoon steady state. Although there are two maxima of precipitation, the monsoonal maximum is very weak and does not coincide with a TCZ. This is not surprising considering the role of the boundary layer in creating two distinct TCZs in the mean state of the control runs [see section 3a(1)].

Second, we investigate whether the mean state of

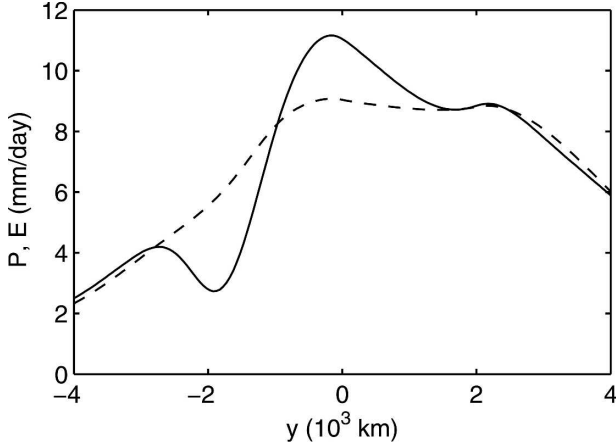


FIG. 15. Precipitation (solid) and evaporation (dashed) produced by the QTCM1.

LC1 is unstable when the perturbations from the mean state are constrained to follow the QTCM1-type profiles. One hypothesis might be that the second degree of freedom is necessary to obtain a realistic mean state, but that the dynamics of the oscillation actually involve only 1 degree of freedom. To test this hypothesis, we use the linear model introduced in section 3d. In this model, we tie the perturbation boundary layer wind, humidity, and temperature to their free-tropospheric counterparts:

$$\begin{aligned} \mathbf{v}'_b &= \mathbf{v}'_0 + V_{1b}\mathbf{v}'_1, \\ s'_b &= a_{1b}T'_1, \quad \text{and} \\ q'_b &= b_{1b}q'_1, \end{aligned} \quad (8)$$

where the primes indicate the perturbations from the mean state. In practice, we will use the surface values of the perturbation profiles in QTCM1 for the parameters V_{1b} , a_{1b} , and b_{1b} . Sensitivity studies have shown that the results are not very sensitive to these parameters.

We can further rewrite the perturbation fields with the vertical structure similar to that of QTCM1:

$$\begin{aligned} \mathbf{v}'(x, y, p, t) &= \tilde{\mathbf{v}}'_0(x, y, t) + \tilde{V}_1(p)\tilde{\mathbf{v}}'_1(x, y, t), \\ T'(x, y, p, t) &= \tilde{a}_1(p)\tilde{T}'_1(x, y, t), \quad \text{and} \\ q'(x, y, p, t) &= \tilde{b}_1(p)\tilde{q}'_1(x, y, t) \end{aligned} \quad (9)$$

for $p_t < p < p_s$, where $\tilde{\mathbf{v}}'_0$ is the troposphere-deep barotropic perturbation wind (with no meridional component in an axisymmetric framework) and $\tilde{\mathbf{v}}'_1$ is the corresponding first baroclinic perturbation wind associated with a modified baroclinic vertical profile $\tilde{V}_1(p)$ that has a zero integral over the troposphere:

$$\int_{p_t}^{p_s} \tilde{V}_1(p) dp = 0. \quad (10)$$

The expressions in Eq. (9) must match the previous notations for perturbations with the constraints (8). This yields the following conditions for $\tilde{\mathbf{v}}'_0$ and $\tilde{\mathbf{v}}'_1$:

$$\tilde{\mathbf{v}}'_0 + \tilde{V}_1(p)\tilde{\mathbf{v}}'_1 = \tilde{\mathbf{v}}'_0 + V_1(p)\mathbf{v}'_1 \quad \text{for } p_t < p < p_e, \quad \text{and} \quad (11)$$

$$= \tilde{\mathbf{v}}'_0 + V_{1b}\mathbf{v}'_1 \quad \text{for } p_e < p < p_s. \quad (12)$$

Averaging the previous equation over the troposphere using condition (10) leads to

$$\tilde{\mathbf{v}}'_0 = \tilde{\mathbf{v}}'_0 + \bar{\mu}V_{1b}\mathbf{v}'_1, \quad (13)$$

where $\bar{\mu} = \mu(1 + \mu)^{-1}$. Subtracting this average from Eq. (11) and separating variables yields the following relationship between $\tilde{\mathbf{v}}'_1$ and \mathbf{v}'_1 :

$$\tilde{\mathbf{v}}'_1 = \mathbf{v}'_1, \quad (14)$$

and the expression of the vertical profile $\tilde{V}_1(p)$:

$$\begin{aligned} \tilde{V}_1(p) &= V_1(p) - \bar{\mu}V_{1b} \quad \text{for } p_t < p < p_e \\ &= (1 - \bar{\mu})V_{1b} \quad \text{for } p_e < p < p_s; \end{aligned} \quad (15)$$

$\tilde{a}_1(p)$ and $\tilde{b}_1(p)$ are extended perturbation functions with the following straightforward expressions:

$$\begin{aligned} \tilde{a}_1(p) &= a_1(p) \quad \text{and} \quad \tilde{b}_1(p) = b_1(p) \quad \text{for } p_t < p < p_e, \\ \tilde{a}_1(p) &= a_{1b} \quad \text{and} \quad \tilde{b}_1(p) = b_{1b} \quad \text{for } p_e < p < p_s. \end{aligned} \quad (16)$$

To sum up, the perturbations relate simply to the tilde perturbations:

$$\begin{aligned} \mathbf{v}'_0 &= \tilde{\mathbf{v}}'_0 - \bar{\mu}V_{1b}\mathbf{v}'_1, \\ \mathbf{v}'_1 &= \tilde{\mathbf{v}}'_1, \\ T'_1 &= \tilde{T}'_1, \quad \text{and} \\ q'_1 &= \tilde{q}'_1. \end{aligned} \quad (17)$$

As in QTCM1, the budget of momentum, energy, and water for the entire column gives the tendency of the barotropic mode $\tilde{\mathbf{v}}'_0$, the temperature \tilde{T}'_1 , and the humidity \tilde{q}'_1 . The budget of momentum weighted by $\tilde{V}_1(p)$ integrated over the troposphere gives the tendency of the baroclinic mode $\tilde{\mathbf{v}}'_1$:

$$\begin{aligned} (1 + \mu)\partial_t\tilde{\mathbf{v}}'_0 &= \mu\partial_t\mathbf{v}'_b + \partial_t\mathbf{v}'_0, \\ (1 + \mu)\langle\tilde{V}_1^2\rangle\partial_t\tilde{\mathbf{v}}'_1 &= \langle V_1^2\rangle^F\partial_t\mathbf{v}'_1 + \bar{\mu}V_{1b}(\partial_t\mathbf{v}'_b - \partial_t\mathbf{v}'_0), \\ (1 + \mu)\langle\tilde{a}_1\rangle\partial_t\tilde{T}'_1 &= \langle a_1\rangle^F\partial_tT'_1 + \mu\partial_t s'_b, \quad \text{and} \\ (1 + \mu)\langle\tilde{b}_1\rangle\partial_t\tilde{q}'_1 &= \langle b_1\rangle^F\partial_tq'_1 + \mu\partial_tq'_b, \end{aligned} \quad (18)$$

where $\partial_t\mathbf{v}'_b$, $\partial_t\mathbf{v}'_0$, $\partial_t\mathbf{v}'_1$, $\partial_tT'_1$, $\partial_t s'_b$, $\partial_tq'_1$, and $\partial_tq'_b$ can be replaced with linearized versions of their expressions in Eqs. (A8)–(A16). Here $\langle\rangle$ indicates the tropospheric average, and average coefficients $\langle\tilde{V}_1^2\rangle$, $\langle\tilde{a}_1\rangle$, and $\langle\tilde{b}_1\rangle$ can be deduced from integrating Eqs. (15) and (16):

TABLE 2. Characteristics and stability of the modified linear models. C: prognostic variables computed as in the QTCM2; T: variables tied to the corresponding free-tropospheric variable as in the QTCM1.

Run	\mathbf{v}_b	q_b	s_b	Stability	Period
T_{BL}	T	T	T	Stable	—
$T_{\mathbf{v}_b}$	T	C	C	Stable	—
$T_{s_b q_b}$	C	T	T	Stable	—
T_{q_b}	C	T	C	Stable	—
T_{s_b}	C	C	T	Unstable	60.9 days

$$\begin{aligned}
 (1 + \mu)\langle \tilde{V}_1^2 \rangle &= \langle V_1^2 \rangle^F + \tilde{\mu} V_{1b}^2, \\
 (1 + \mu)\langle \tilde{a}_1 \rangle &= \langle a_1 \rangle^F + \mu a_{1b}, \quad \text{and} \\
 (1 + \mu)\langle \tilde{b}_1 \rangle &= \langle b_1 \rangle^F + \mu b_{1b}. \quad (19)
 \end{aligned}$$

Although the reference and perturbation structure functions of this hybrid model are different from QTCM1 in the boundary layer, the essential nature of the QTCM1 is reproduced for the perturbation from the QTCM2 mean state. The eigenvalues and eigenvectors of the Jacobian of this model are computed using the same spatial resolution (400 points). This linear model (hereafter, run T_{BL}) has no linearly unstable mode. This result shows that the second degree of freedom in QTCM2 is crucial to the dynamics of the instability itself, not only to establish an unstable mean state.

We further develop modified versions of the model to determine in which vertical structures this second degree of freedom is necessary. We perform computations of eigenvalues and eigenvectors for models where (i) only the ABL wind \mathbf{v}_b is tied to the free-tropospheric flow (run $T_{\mathbf{v}_b}$), (ii) s_b and q_b are tied to the free-tropospheric profiles (run $T_{s_b q_b}$), (iii) only q_b is tied to the free-tropospheric humidity (run T_{q_b}), and (iv) only s_b is tied to the free-tropospheric temperature (run T_{s_b}). Table 2 sums up the different computations.

In cases $T_{\mathbf{v}_b}$, $T_{s_b q_b}$, and T_{q_b} , the mean state is stable: all the eigenvalues of the Jacobian have negative real parts. In case T_{s_b} , the basic state is unstable, and the one unstable mode is oscillatory. Its period is 60.9 days and its e -folding time is 50.9 days, close to the characteristics of the QTCM2 unstable mode (63.3 and 51.5 days). The amplitude and phase of precipitation for the T_{s_b} unstable mode are shown in Fig. 16. They are almost identical to those of the QTCM2 linearly unstable mode, and very similar to the structure of the first harmonic of LC1.

These experiments show that the second degree of freedom in the vertical structure is necessary in both the humidity and the wind profiles to obtain the model northward-propagating oscillation. This suggests that moisture-convection feedbacks are crucial to the devel-

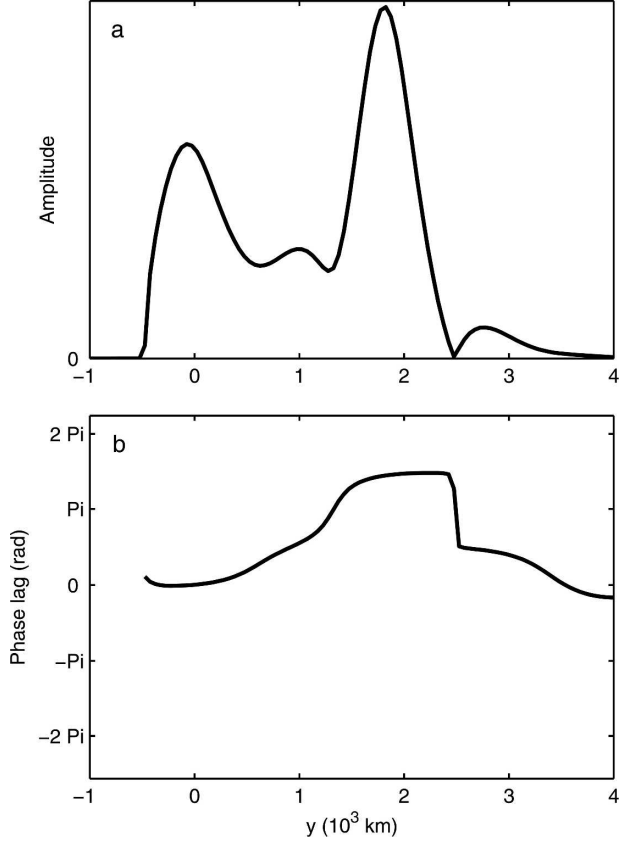


FIG. 16. (a) Amplitude and (b) phase of the unstable mode of T_{s_b} .

opment of this oscillation. Moreover, these experiments show that the QTCM2 is close to the simplest model of this phenomenon.

4. Conclusions

We used an intermediate-complexity axisymmetric model to investigate the dynamics of poleward-propagating disturbances, with an aim toward understanding the intraseasonal variability of the Asian monsoon. Our model has a prognostic boundary layer, coupled to a free troposphere with two vertical modes in velocity and one each in temperature and humidity, and a quasi-equilibrium convective closure. The lower boundary condition is fixed SST, with a latitudinal profile similar to that observed in the Bay of Bengal in northern summer. The main results are as follows:

- 1) The simulated dynamical and thermodynamical seasonal mean fields are similar to the observations.
- 2) The model exhibits two limit cycles with similar structures and periods in the 30–60-day range. The structure in precipitation, divergence, and vorticity

of both cycles is similar to composites of observations: the precipitation lags a maximum of barotropic divergence preceded by a maximum of barotropic vorticity.

- 3) These results show that northward propagation of the TCZ can arise from the instability of the monsoon flow and can exist independently of longitudinal propagation. A linearized version of the model shows that the dynamics of this instability are essentially linear.
- 4) In our model, the 30–60-day oscillation results from atmospheric-only processes, independent of the coupling with continental surfaces or an interactive ocean, except as those may be implicit in the mean state, which here is determined by our assumed SST distribution. The inclusion of the wind–evaporation effect in the parameterization of surface fluxes is nevertheless necessary.
- 5) The boundary layer flow and humidity play crucial roles in the instability of the mean flow. The mean monsoon flow is not linearly unstable if either the ABL flow or humidity is tied to the free-tropospheric profiles.

The main interest of this work resides in the introduction of a model that is relatively simple and, at the same time, is able to produce both a seasonal mean and an intraseasonal oscillation that are similar to the zonally averaged observed mean monsoon flow and boreal summer 30–60-day intraseasonal mode. This study also highlights the role of the wind–evaporation feedback in the instability of the mean flow, a process that did not appear crucial in other recent modeling studies (Drbohlav and Wang 2005; Jiang et al. 2004). This latter result suggests the hypothesis that the same feedback may be essential to the observed oscillation.

Our model also appears to be one of the simplest models that can attain these results. The 2 degrees of freedom in the vertical profiles of moisture and momentum appear necessary to the development of the simulated intraseasonal oscillation. The suppression of the second degree of freedom in either profile cancels some of the moisture–convection–dynamics feedbacks crucial to the instability of the mean monsoon flow. Our model is therefore a basic tool to reach a better theoretical understanding of the 30–60-day oscillation. Nevertheless, despite the simplicity of the model, the mechanisms at play in the northward propagation of the TCZ are complex and require further work.

Previous axisymmetric modeling studies (Webster and Chou 1980; Webster 1983; Srinivasan et al. 1993; Nanjundiah et al. 1992) used simpler models (with no dynamical boundary layer), and simulated an intrasea-

sonal oscillation. In these models, land–atmosphere interaction was crucial to the oscillation. In our model, the 30–60-day oscillation appears as an instability of the monsoon axisymmetric flow that results from atmospheric processes only: from the interaction of convection and dynamics. This is consistent with previous studies using GCMs (Goswami and Shukla 1984), and its relevance is upheld by recent composite analyses that highlight the importance of the boundary layer flow (Kemball-Cook and Wang 2001; Lawrence and Webster 2002; Jiang et al. 2004). The mechanisms of the instability in our model are also different from those in the model used by Drbohlav and Wang (2005): while the wind-induced surface fluxes are crucial to the development of the oscillation in our model, surface fluxes are not taken into account in Drbohlav and Wang (2005). Their parameterization of rainfall is based on the precipitation of a fraction of the convergence of humidity (Kuo 1974); this suggests that the instability mechanism in their model is similar to the conditional instability of the second kind.

Because the main characteristics of the model intraseasonal oscillation are determined by linear dynamics, it should be possible to use the linearized version of the model to investigate the main mechanisms that cause the instability of the mean flow. In particular, discriminating the role of the mean flow from the sensitivity to different parameters is a possible development. Future work will address this topic.

Acknowledgments. This work was supported by a fellowship from the David and Lucile Packard Foundation, and NSF Grant ATM-05-42736. The authors would like to thank D. Neelin for constantly helping to improve the model. We acknowledge fruitful discussions with W. Boos, K. Emanuel, O. Pauluis, and J. Srinivasan.

APPENDIX

Model Description

a. Vertical profiles

In the QTCM2, the temperatures and humidity are expressed in energy units; that is, temperature in Kelvin multiplied by the heat capacity of air at constant pressure C_p and specific humidity in kg kg^{-1} multiplied by the latent heat of vaporization L_v .

In the free troposphere, the horizontal wind $\mathbf{v} = (u, v)$, temperature T , and humidity q are expressed as follows:

$$\begin{aligned} \mathbf{v}(x, y, p, t) &= V_0(p)\mathbf{v}_0(x, y, t) + V_1(p)\mathbf{v}_1(x, y, t), \\ T(x, y, p, t) &= T_r(p) + a_1(p)T_1(x, y, t), \quad \text{and} \\ q(x, y, p, t) &= q_r(p) + b_1(p)q_1(x, y, t) \end{aligned} \quad (\text{A1})$$

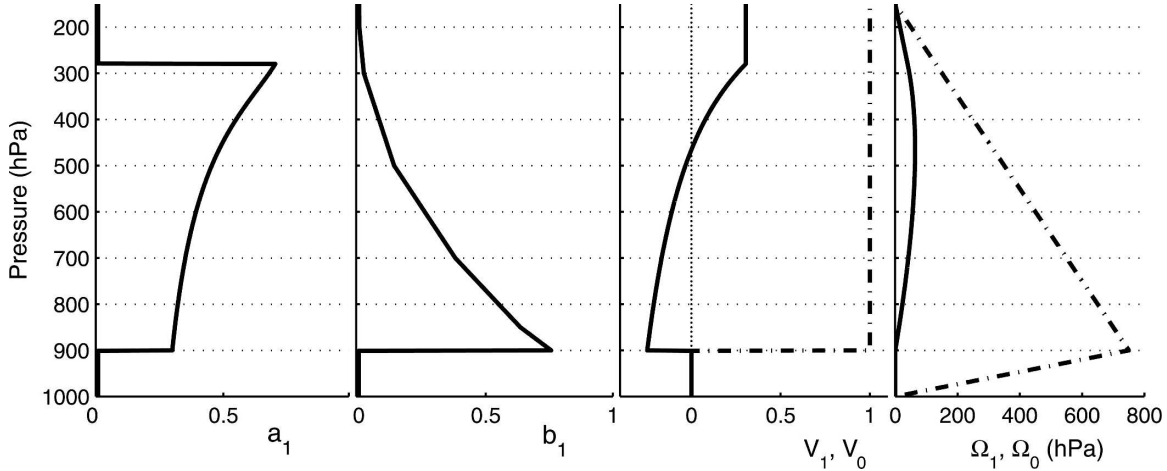


FIG. A1. Free-tropospheric basis functions for temperature a_1 and humidity b_1 , horizontal wind V_0 (dash-dotted) and V_1 (solid), and vertical wind Ω_0 (dash-dotted) and Ω_1 (solid).

for $p_t < p < p_e$, where p_t is the pressure at the tropopause and p_e is the pressure at the top of the ABL; $T_r(p)$ and $q_r(p)$ are reference profiles [$T_r(p)$ follows a moist adiabat], $b_1(p)$ is the perturbation structure function for humidity and the perturbation structure function for temperature $a_1(p)$ is the perturbation of the moist adiabat up to 280 mb, above which cold top effects are considered to cancel the moist adiabatic perturbation (Holloway and Neelin 2007). These free-tropospheric reference profiles are the same as in QTCM1 (Zeng et al. 2000), but modified to begin at the top of the ABL rather than at the nominal surface. The profile for barotropic velocity, $V_0(p)$, is constant in pressure: $V_0(p) = 1$. The profile for baroclinic velocity, $V_1(p)$, is constructed to be consistent with a_1 , assuming that the pressure gradient force obtained from a_1 by hydrostatic balance has the same vertical structure as the other linear terms in the momentum equation. Figure A1 shows the perturbation profiles a_1 , b_1 and the wind profiles V_0 , V_1 .

To ensure mass continuity, the vertical velocity can be written

$$\omega(x, y, p, t) = -\Omega_0(p)\nabla \cdot \mathbf{v}_0(x, y, t) - \Omega_1(p)\nabla \cdot \mathbf{v}_1(x, y, t), \quad (\text{A2})$$

where

$$\Omega_i(p) = \int_{p_t}^p V_i(p) dp \quad \text{for } p_t < p < p_e. \quad (\text{A3})$$

Here V_0 's expression gives $\Omega_0(p) = p - p_t$, and because V_1 represents the baroclinic mode $\Omega_1(p_e) = 0$. Figure A1 shows Ω_0 and Ω_1 ; there the former is completed for $p > p_e$ by the corresponding boundary layer mode.

The ABL is considered well mixed. There, \mathbf{v} , q , and the dry static energy s are expressed as

$$\begin{aligned} \mathbf{v}(x, y, p, t) &= \mathbf{v}_b(x, y, t), \\ s(x, y, p, t) &= s_{rb} + s_b(x, y, t), \quad \text{and} \\ q(x, y, p, t) &= q_{rb} + q_b(x, y, t) \end{aligned} \quad (\text{A4})$$

for $p_e < p < p_s$, where p_s is the pressure at the surface; s_{rb} and q_{rb} are reference values for ABL dry static energy and specific humidity. The temperature follows a dry adiabat, and can therefore be computed from s . To ensure mass continuity, the vertical velocity in the ABL can be written as

$$\omega(x, y, p, t) = (p_s - p)\nabla \cdot \mathbf{v}_b(x, y, t), \quad (\text{A5})$$

and at p_e we have $\omega(x, y, p_e, t) = (p_s - p_e)\nabla \cdot \mathbf{v}_b(x, y, t) = -(p_e - p_t)\nabla \cdot \mathbf{v}_0(x, y, t)$, which yields

$$p_B \nabla \cdot \mathbf{v}_b(x, y, t) = -p_F \nabla \cdot \mathbf{v}_0(x, y, t), \quad (\text{A6})$$

where $p_F = p_e - p_t$ is the depth of the free troposphere and $p_B = p_s - p_e$ is the depth of the ABL. Furthermore, since the model is axisymmetric, $\nabla \cdot \mathbf{v} = \partial_y v$. By integrating from the extremity of the domain (the equatorial β plane's "pole") we can further write

$$\mu v_b(x, y, t) = -v_0(x, y, t), \quad (\text{A7})$$

with $\mu = p_B/p_F$.

b. Model equations

For the free troposphere, we assume the vertical structures described above and perform vertical integrations to obtain the model equations, essentially a low-order Galerkin truncation. The model temperature, moisture, and barotropic momentum equations are obtained by vertical averaging of the respective three-dimensional equations over the free troposphere for those variables, while the baroclinic equation is obtained by first multiplying the momentum equation by $V_1(p)$ and then averaging. The equations can be written in either flux or advective form, with no significant con-

sequences. As in Sobel and Neelin (2006), we write the equations for the boundary layer variables and the free-tropospheric barotropic velocity in flux form, while we write the equations for free-tropospheric tem-

perature, moisture, and baroclinic velocity in advective form.

The resulting free-tropospheric temperature and moisture equations are

$$\begin{aligned} \langle a_1 \rangle^F (\partial_t T_1 + \mathbf{v}_0 \cdot \nabla T_1) + M_{s0} \nabla \cdot \mathbf{v}_0 + \langle a_1 V_1 \rangle^F \mathbf{v}_1 \cdot \nabla T_1 + M_{s1} \nabla \cdot \mathbf{v}_1 - (\nabla \cdot \mathbf{v}_0) (s^\dagger - s_e) \\ = \langle Q_c \rangle^F + \langle Q_R \rangle^F + \langle a_1 \rangle^F k_q \nabla^2 T_1, \quad \text{and} \end{aligned} \quad (\text{A8})$$

$$\langle b_1 \rangle^F (\partial_t q_1 + \mathbf{v}_0 \cdot \nabla q_1) - M_{q0} \nabla \cdot \mathbf{v}_0 + \langle b_1 V_1 \rangle^F \mathbf{v}_1 \cdot \nabla q_1 + M_{q1} \nabla \cdot \mathbf{v}_1 - (\nabla \cdot \mathbf{v}_0) (q^\dagger - q_e) = \langle Q_q \rangle^F + \langle b_1 \rangle^F k_q \nabla^2 q_1, \quad (\text{A9})$$

where $\langle \rangle^F$ indicates the free-tropospheric average. The subscript “e” indicates the value just above ABL top, and the superscript “†” indicates the value used to calculate the vertical advection at the boundary layer top. Here Q_c , Q_q , and Q_R are the convective heating, convective moistening, and radiative heating, respectively, and k_q is the horizontal diffusivity coefficient for humidity and temperature. We have further defined the

gross dry static stabilities and gross moisture stratifications for each mode:

$$\begin{aligned} M_{si} &= M_{sri} + M_{spi} T_1 = -\langle \Omega_i \partial_p s_r \rangle^F - \langle \Omega_i \partial_p (a_1 + \kappa a_1^+) \rangle^F T_1, \\ M_{qi} &= M_{qri} + M_{qpi} q_1 = \langle \Omega_i \partial_p q_r \rangle^F + \langle \Omega_i \partial_p b_1 \rangle^F q_1, \end{aligned} \quad (\text{A10})$$

where the index i can be either 0 or 1.

The equations for barotropic and baroclinic velocities are

$$\partial_t \mathbf{v}_0 + \nabla \cdot (\mathbf{v}_0 \mathbf{v}_0) + \langle V_1^2 \rangle^F \nabla \cdot (\mathbf{v}_1 \mathbf{v}_1) - (\nabla \cdot \mathbf{v}_0) \mathbf{v}^\dagger + f \hat{\mathbf{k}} \times \mathbf{v}_0 = -\nabla (\kappa a_b^+ s_b + \kappa \langle a_1^+ \rangle^F T_1 + \phi_s) + k_v \nabla^2 \mathbf{v}_0, \quad \text{and} \quad (\text{A11})$$

$$\begin{aligned} \partial_t \mathbf{v}_1 + \mathbf{v}_0 \cdot \nabla \mathbf{v}_1 + \mathbf{v}_1 \cdot \nabla \mathbf{v}_0 + \frac{\langle V_1^3 \rangle^F}{\langle V_1^2 \rangle^F} \mathbf{v}_1 \cdot \nabla \mathbf{v}_1 + \frac{\langle V_1^3 \rangle^F}{2 \langle V_1^2 \rangle^F} (\nabla \cdot \mathbf{v}_1) \mathbf{v}_1 - \frac{1}{2} \left(\frac{V_{1e}}{\langle V_1^2 \rangle^F} - 1 \right) (\nabla \cdot \mathbf{v}_0) \mathbf{v}_1 - \frac{V_{1e}}{\langle V_1^2 \rangle^F} (\nabla \cdot \mathbf{v}_0) (\mathbf{v}^\dagger - \mathbf{v}_e) \\ + f \hat{\mathbf{k}} \times \mathbf{v}_1 = -\kappa \nabla T_1 - \epsilon_1 \mathbf{v}_1 + k_v \nabla^2 \mathbf{v}_1, \end{aligned} \quad (\text{A12})$$

where $f = \beta y$ is the Coriolis parameter, $\hat{\mathbf{k}}$ is the vertical unit vector, $\kappa = R/C_p$ is the ratio of the gas constant for air R by the heat capacity of air at constant pressure C_p , ϕ_s is the surface geopotential, k_v is the horizontal diffusivity coefficient for momentum, and ϵ_1 is a coefficient that accounts for vertical mixing by small eddies. We have also introduced the notational shorthand $V_{1e} \equiv V_1(p_e)$. The coefficients a_b^{+e} and a_1^+ come from integrating temperature to obtain geopotential using hydrostatic balance, and they are defined by

$$\begin{aligned} a_b^{+e} &= \int_{p_e}^{p_s} a_b d \ln p = a_b^+(p_e), \quad \text{and} \\ a_1^+(p) &= \int_p^{p_e} a_1(p') d \ln p'. \end{aligned} \quad (\text{A13})$$

For the boundary layer, the procedure is essentially the same but simpler, as each variable has only one

mode, and each prognostic variable q , s , or \mathbf{v} is assumed uniform on the vertical. We thus have the following equations for ABL dry static energy and specific humidity:

$$\begin{aligned} \partial_t s_b + \nabla \cdot [\mathbf{v}_b (s_{rb} + s_b)] - s^\dagger \nabla \cdot \mathbf{v}_b \\ = \frac{g}{p_B} H + \langle Q_R \rangle^b + \langle Q_c \rangle^b + k_q \nabla^2 s_b, \quad \text{and} \end{aligned} \quad (\text{A14})$$

$$\begin{aligned} \partial_t q_b + \nabla \cdot [\mathbf{v}_b (q_{rb} + q_b)] - q^\dagger \nabla \cdot \mathbf{v}_b \\ = \frac{g}{p_B} E + \langle Q_q \rangle^b + k_q \nabla^2 q_b. \end{aligned} \quad (\text{A15})$$

Here E and H are the surface fluxes of latent and sensible heat, respectively, and $\langle \rangle^b$ indicates averaging over the boundary layer.

The ABL velocity obeys the equation

$$\begin{aligned} \partial_t \mathbf{v}_b + \nabla \cdot (\mathbf{v}_b \mathbf{v}_b) - \mathbf{v}^\dagger \nabla \cdot \mathbf{v}_b + f \hat{\mathbf{k}} \times \mathbf{v}_b \\ = -\nabla (\kappa \langle a_b^+ \rangle^b s_b + \phi_s) - \epsilon_b \mathbf{v}_b + k_v \nabla^2 \mathbf{v}_b, \end{aligned} \quad (\text{A16})$$

where ϵ_b is a surface drag coefficient. The coefficient of the baroclinic ABL geopotential contribution $\langle a_b^+ \rangle^b$ results from the integration to obtain the geopotential:

$$\langle a_b^+ \rangle^b = p_B^{-1} \int_{p_e}^{p_s} \int_p^{p_s} a_b d \ln p dp. \quad (\text{A17})$$

Terms involving s^\dagger , q^\dagger , or \mathbf{v}^\dagger represent vertical advective fluxes at the ABL top. We choose to use an upwind formulation of these terms:

$$\begin{aligned} X^\dagger &= X_{rb} + X_b \quad \text{if } \nabla \cdot \mathbf{v}_b < 0, \quad \text{and} \\ X^\dagger &= X_e \quad \text{if } \nabla \cdot \mathbf{v}_b > 0, \end{aligned}$$

with $X = s, q$, or \mathbf{v} ($\mathbf{v}_{rb} = 0$). A centered formulation was also proposed in Sobel and Neelin (2006):

$$X^\dagger = \frac{1}{2} (X_{rb} + X_b + X_e).$$

This latter formulation will be used in the linear model (section 3d).

Using the continuity equation [Eq. (A7)], the surface geopotential gradient $\partial_y \phi_s$ can be diagnosed by adding the meridional components of Eqs. (A11) and (A16) weighted by the depth of the corresponding layer. The resulting expression for the surface geopotential is

$$\begin{aligned} (1 + \mu) \partial_y \phi_s &= -\kappa \partial_y [(\mu \langle a_b^+ \rangle^b + a_b^+ e) s_b + \langle a_1^+ \rangle^F T_1] \\ &\quad - f(\mu u_b + u_0) - \epsilon_b \mu v_b - \mu(1 + \mu) \partial_y (v_b^2) \\ &\quad - \langle V_1^2 \rangle^F \partial_y (v_1^2). \end{aligned} \quad (\text{A18})$$

In practice, Eq. (A18) is used with Eq. (A16) to compute v_b , and u_0 is diagnosed from v_b using the continuity equation [Eq. (A7)].

c. Model physics

1) CONVECTION

The convective heating and moistening $\langle Q_c \rangle^F$, $\langle Q_c \rangle^b$, $\langle Q_q \rangle^F$, and $\langle Q_q \rangle^b$ are parameterized using the Betts–Miller scheme (Betts 1986; Betts and Miller 1986) as implemented in the prototype QTCM2 (Sobel and Neelin 2006). In the Betts–Miller scheme, precipitation is proportional to the convective available potential energy \mathcal{E} of the column if the latter is positive, and is zero otherwise. In the current version of the model, we use the following reference profiles:

$$T^c(p) = T_r(p) + a_1(p)(h_b + \delta h_b), \quad \text{and} \quad (\text{A19})$$

$$q^c(p) = q_r(p) + b_1(p)(h_b + \delta h_b), \quad (\text{A20})$$

where $h_b = s_b + q_b$ and δh_b is an adjustment variable that allows energy conservation and some downdraft effects. This yields the following expression for the convective available potential energy:

$$\mathcal{E} = p_F \langle a_1 \rangle^F (h_b + \delta h_b - T_1) + p_B \sigma \delta h_b, \quad (\text{A21})$$

where σ is a parameter that partitions the convective cooling and drying in the boundary layer.

The convective contributions to the energy and water budgets are

$$\begin{aligned} \langle Q_c \rangle^F &= \mathcal{H}(\mathcal{E}) \epsilon_c \langle a_1 \rangle^F (h_b + \delta h_b - T_1), \\ \langle Q_q \rangle^F &= \mathcal{H}(\mathcal{E}) \epsilon_c \langle b_1 \rangle^F (h_b + \delta h_b - q_1), \\ \langle Q_c \rangle^b &= \mathcal{H}(\mathcal{E}) \epsilon_c \sigma \delta h_b, \quad \text{and} \\ \langle Q_q \rangle^b &= \mathcal{H}(\mathcal{E}) \epsilon_c (1 - \sigma) \delta h_b, \end{aligned} \quad (\text{A22})$$

where $\epsilon_c = \tau_c^{-1}$ is a large damping rate for the dissipation of buoyancy by convection and \mathcal{H} is the Heaviside step function [$\mathcal{H}(x) = 0$ if $x < 0$, $\mathcal{H}(x) = 1$ if $x > 0$].

To obtain δh_b , we apply the energy constraint that the net moisture loss must equal the net (dry) enthalpy gain:

$$p_B (\langle Q_c \rangle^b + \langle Q_q \rangle^b) + p_F (\langle Q_c \rangle^F + \langle Q_q \rangle^F) = 0, \quad (\text{A23})$$

which yields the following expression for δh_b :

$$\delta h_b = \frac{[-\langle a_1 \rangle^F + \langle b_1 \rangle^F] h_b + \langle a_1 \rangle^F T_1 + \langle b_1 \rangle^F q_1}{\mu + \langle a_1 \rangle^F + \langle b_1 \rangle^F}. \quad (\text{A24})$$

Condensed water is considered to precipitate immediately, and the precipitation is therefore

$$\begin{aligned} P &= -(p_B \langle Q_q \rangle^b + p_F \langle Q_q \rangle^F) = p_B \langle Q_c \rangle^b + p_F \langle Q_c \rangle^F \\ &= \epsilon_c \mathcal{H}(\mathcal{E}) \mathcal{E}. \end{aligned} \quad (\text{A25})$$

2) RADIATION

In the free troposphere, we use a Newtonian cooling:

$$\langle Q_R \rangle^F = \frac{T_R - T_1}{\tau_R}, \quad (\text{A26})$$

where T_R is a radiative equilibrium temperature (relative to the reference temperature T_r) and τ_R a radiative time scale.

In the boundary layer, we use the scheme

$$\langle Q_R \rangle^b = Q_{Rb0} + \frac{T_s - s_{rb} - s_b}{\tau_{Rb}}, \quad (\text{A27})$$

where Q_{Rb0} is a negative constant and τ_{Rb} is the time scale on which the boundary layer is relaxed toward the

SST by radiative processes alone, estimated from linearization of a graybody scheme.

REFERENCES

- Bellenger, H., and J.-P. Duvel, 2007: Intraseasonal convective perturbations related to the seasonal march of the Indo-Pacific monsoons. *J. Climate*, **20**, 2853–2863.
- Bellon, G., and J. Srinivasan, 2006: Comments on “Structures and mechanisms of the northward propagating boreal summer intraseasonal oscillation.” *J. Climate*, **19**, 4738–4743.
- Betts, A. K., 1986: A new convective adjustment scheme. Part I: Observational and theoretical basis. *Quart. J. Roy. Meteor. Soc.*, **112**, 677–691.
- , and M. J. Miller, 1986: A new convective adjustment scheme. Part II: Single column tests using GATE wave, BOMEX, ATEX and arctic air-mass data sets. *Quart. J. Roy. Meteor. Soc.*, **112**, 693–709.
- Burns, S. P., A. H. Sobel, and L. M. Polvani, 2006: Asymptotic solutions of the axisymmetric moist Hadley circulation in a model with two vertical modes. *Theor. Comput. Fluid Dyn.*, **20**, 443–467.
- Chatterjee, P., and B. N. Goswami, 2004: Structure, genesis and scale selection of the tropical quasi-biweekly mode. *Quart. J. Roy. Meteor. Soc.*, **130**, 1171–1194.
- Drbohlav, H.-K. L., and B. Wang, 2005: Mechanism of the northward-propagating intraseasonal oscillation: Insights from a zonally symmetric model. *J. Climate*, **18**, 952–972.
- Emanuel, K. A., 1987: An air-sea interaction model of intraseasonal oscillations in the Tropics. *J. Atmos. Sci.*, **44**, 2324–2340.
- Fu, X., and B. Wang, 2004: Differences of boreal summer intraseasonal oscillations simulated in an atmosphere–ocean coupled model and an atmosphere-only model. *J. Climate*, **17**, 1263–1271.
- Gadgil, S., and J. Srinivasan, 1990: Low frequency variation of tropical convergence zones. *Meteor. Atmos. Phys.*, **44**, 119–132.
- , and P. R. S. Rao, 2000: Famine strategies for a variable climate—A challenge. *Curr. Sci.*, **78**, 1203–1215.
- Goswami, B. N., 2005: South Asian monsoon. *Intraseasonal Variability in the Atmosphere–Ocean Climate System*, W. K. M. Lau and D. E. Waliser, Eds., Springer-Verlag, 19–61.
- , and J. Shukla, 1984: Quasi-periodic oscillations in a symmetric general circulation model. *J. Atmos. Sci.*, **41**, 20–37.
- , and R. S. A. Mohan, 2001: Intraseasonal oscillations and interannual variability of the Indian summer monsoon. *J. Climate*, **14**, 1180–1198.
- Holloway, C. E., and J. D. Neelin, 2007: The convective cold top and quasi equilibrium. *J. Atmos. Sci.*, **64**, 1467–1487.
- Jiang, X., and T. Li, 2005: Reinitiation of the boreal summer intraseasonal oscillation in the tropical Indian Ocean. *J. Climate*, **18**, 3777–3795.
- , —, and B. Wang, 2004: Structures and mechanisms of the northward propagating boreal summer intraseasonal oscillation. *J. Climate*, **17**, 1022–1039.
- Kemball-Cook, S., and B. Wang, 2001: Equatorial waves and air–sea interaction in the boreal summer intraseasonal oscillation. *J. Climate*, **14**, 2923–2942.
- Kuo, H. L., 1974: Further studies of the parameterization of the influence of cumulus convection on large-scale flow. *J. Atmos. Sci.*, **31**, 1232–1240.
- Lawrence, D. M., and P. Webster, 2002: The boreal summer intraseasonal oscillation: Relationship between northward and eastward movement of convection. *J. Atmos. Sci.*, **59**, 1593–1606.
- Maloney, E., and A. H. Sobel, 2004: Surface fluxes and ocean coupling in the tropical intraseasonal oscillation. *J. Climate*, **17**, 4368–4386.
- Mapes, B. E., P. Liu, and N. Buening, 2005: Indian monsoon onset and the Americas midsummer drought: Out-of-equilibrium responses to smooth seasonal forcing. *J. Climate*, **18**, 1109–1115.
- Nanjundiah, R., J. Srinivasan, and S. Gadgil, 1992: Intraseasonal variation of the Indian summer monsoon. Part II: Theoretical aspects. *J. Meteor. Soc. Japan*, **70**, 529–550.
- Neelin, J. D., and N. Zeng, 2000: A quasi-equilibrium tropical circulation model—Formulation. *J. Atmos. Sci.*, **57**, 1741–1766.
- , I. M. Held, and K. H. Cook, 1987: Evaporation–wind feedback and low-frequency variability in the tropical atmosphere. *J. Atmos. Sci.*, **44**, 2341–2348.
- Pauluis, O., 2004: Boundary layer dynamics and cross-equatorial Hadley circulation. *J. Atmos. Sci.*, **61**, 1161–1173.
- Sengupta, D., B. N. Goswami, and R. Senan, 2001: Coherent intraseasonal oscillations of ocean and atmosphere during the Asian summer monsoon. *Geophys. Res. Lett.*, **28**, 4127–4130.
- Sikka, D. R., and S. Gadgil, 1980: On the maximum cloud zone and the ITCZ over Indian longitudes during the southwest monsoon. *Mon. Wea. Rev.*, **108**, 1840–1853.
- Sobel, A. H., and J. D. Neelin, 2006: The boundary layer contribution to intertropical convergence zones in the quasi-equilibrium tropical circulation model framework. *Theor. Comput. Fluid Dyn.*, **20**, 323–350.
- Srinivasan, J., S. Gadgil, and P. J. Webster, 1993: Meridional propagation of large-scale monsoon convective zones. *Meteor. Atmos. Phys.*, **52**, 15–35.
- Wang, B., and H. Rui, 1990: Synoptic climatology of transient tropical intraseasonal convection anomalies: 1975–1985. *Meteor. Atmos. Phys.*, **44**, 43–61.
- , and X. Xie, 1997: A model for the boreal summer intraseasonal oscillation. *J. Atmos. Sci.*, **54**, 72–86.
- , P. J. Webster, K. Kikuchi, T. Yasunari, and Y. Qi, 2006: Boreal summer quasi-monthly oscillation in the global tropics. *Climate Dyn.*, **27**, 661–675.
- Webster, P. J., 1983: Mechanisms of monsoon low-frequency variability: Surface hydrological effects. *J. Atmos. Sci.*, **40**, 2110–2124.
- , and L. C. Chou, 1980: Low-frequency transitions of a simple monsoon system. *J. Atmos. Sci.*, **37**, 368–382.
- Zeng, N., J. D. Neelin, and C. Chou, 2000: A quasi-equilibrium tropical circulation model—Implementation and simulation. *J. Atmos. Sci.*, **57**, 1767–1796.